

Plasma Production and Parametric Heating by Means
of Electron Plasma Waves in the W II A Stellarator

P. Javel, G. Müller, U. Weber, R.R. Weynants⁺)

IPP 2/229

June 1976



MAX-PLANCK-INSTITUT FÜR PLASMAPHYSIK

8046 GARCHING BEI MÜNCHEN

MAX-PLANCK-INSTITUT FÜR PLASMAPHYSIK
GARCHING BEI MÜNCHEN

Plasma Production and Parametric Heating by Means
of Electron Plasma Waves in the W II A Stellarator

P.Javel, G.Müller, U.Weber, R.R.Weynants⁺)

IPP 2/229

June 1976

⁺) Laboratoire de Physique des Plasmas-Laboratorium voor Plasmafysica
Association "Euratom-Etat belge" - Associatie "Euratom-Belgische Staat"
Ecole Royale Militaire - 1040 Brussels - Koninklijke Militaire School

*Die nachstehende Arbeit wurde im Rahmen des Vertrages zwischen dem
Max-Planck-Institut für Plasmaphysik und der Europäischen Atomgemeinschaft über die
Zusammenarbeit auf dem Gebiete der Plasmaphysik durchgeführt.*

IPP 2/229

P. Javel

G. Müller

U. Weber

R.R. Weynants

Plasma Production and Parametric Heating
by Means of Electron Plasma Waves in the
W II A Stellarator.

June 1976

Abstract

A detailed study is presented of the properties of the plasma sustained by electron plasma waves launched from an electrostatic coupler. The most salient features are the limitation in the density imposed by the applied frequency, the crucial importance of the so-called resonance cones and the close correlation between the observed parametric-decay phenomena and the concomitant ion heating. The resonance cones, in combination with rather short absorption lengths due to the decay, are shown to lead to a rather severe drop in the source efficiency at high power levels. We furthermore discuss the influence of the pump inhomogeneity on the instability growth and the relevance of the present study on actual lower hybrid experiments.

1. Introduction

Several plasma production schemes that sustain the plasma by means of electron plasma waves (also called electron space charge waves) have been proposed in the past [1 - 3], but the mechanisms of wave absorption and subsequent thermalization have remained largely unexplained until very recently [4,5]. The slow wave branch of the cold plasma dispersion relations is given by

$$k_{\perp}^2 = -k_z^2 \frac{(\omega^2 - \omega_{pe}^2) \cdot (\omega^2 - \omega_{ce}^2)}{(\omega^2 - \omega_{LH}^2) \cdot (\omega^2 - \omega_{pe}^2 - \omega_{ce}^2)}, \quad (1)$$

where $k_z \gg \frac{\omega}{c}$, $\omega \gg \omega_{ci}$ and terms of the order of $\frac{m_e}{m_i}$ are neglected with respect to 1. The wavenumbers k_{\perp} and k_z are the components of k perpendicular and parallel to the magnetic field, respectively. Under the condition $\omega_{pi} \gg \omega_{ci}$, the lower hybrid frequency is given by $\omega_{LH} = \omega_{pi} \left(1 + \frac{\omega_{pe}^2}{\omega_{ce}^2}\right)^{-1/2}$, where ω_{pi} and ω_{pe} are the ion and electron plasma frequencies and ω_{ci} and ω_{ce} the ion and electron cyclotron frequencies, respectively. At frequencies close to ω_{LH} , the dispersion equation (1) drastically changes with ω and the waves are commonly called lower hybrid waves.

The existence regions ($k_{\perp}^2 > 0$) of the electron plasma waves as described by Eq. (1) is schematically indicated by the hatched zones in Fig.1. When the quasistatic approximation ($k_z \gg \frac{\omega}{c}$) is fulfilled, the waves can only propagate up to a given point in the hatched region provided k_z exceeds a given value. In particular, the lower hybrid layer can only be reached when

$$\left(\frac{k_z c}{\omega}\right)^2 > \left(1 + \frac{\omega_{pe,o}^2}{\omega_{ce,o}^2}\right),$$

where $\omega_{pe,o}$ and $\omega_{ce,o}$ are the values of ω_{pe} and ω_{ce} taken at the hybrid layer. When the latter condition is fulfilled the lower hybrid is said to be accessible [6,7]. With the above mentioned restrictions one can always find in the hatched region, for given ω , ω_{ce} , ω_{pe} and k_z , a wave

(with $\text{Re } k_{\perp}$ according to Eq.1) via which energy may be coupled into a target plasma. Assuming that the wave absorption and the subsequent thermalization are sufficiently efficient and fast compared with the confinement time, one can easily imagine that a substantial part of the plasma energy content can be supplied by wave energy deposition. The target plasma source can then be turned off and the plasma will be sustained only by the electron plasma waves themselves. This possibility has been borne out experimentally in, for example, Refs. 2 and 3. Furthermore, Ref.2 stresses the fact that the generator-plasma matching problem can be greatly reduced when a bounded plasma resonance can be excited.

Going back to Fig.1, we see that there is no theoretical limit for the density which could be reached when $\frac{\omega_{ce}}{\omega} < \sqrt{\frac{m_i}{m_e}}$. In practice, of course, the confinement characteristics, the power level and the applied k_{\perp} spectrum constitute the real plasma density limitation. For $\frac{\omega_{ce}}{\omega} < \sqrt{\frac{m_i}{m_e}}$, on the other hand, the lower hybrid plasma resonance comes into play and the maximum density which can be reached is such that the corresponding ion plasma frequency equals the applied frequency ($\omega_{pi} = \omega$).

As a scrutiny of the latter region this paper is supplementary to Ref. 8. The unnecessary reduction in density is the price one pays for gaining an insight into the way in which energy might be carried by the electron plasma waves up to the hybrid layer. The most salient features here are the crucial importance of the so-called resonance cones [9] and the parametric decay of the lower hybrid waves. Since, moreover, the experiment is conducted in toroidal geometry, the experimental situation bears relevance to those experiments aiming at heating magnetically confined plasmas to thermonuclear temperatures by radiofrequency power in the lower hybrid frequency range.

High values of $\frac{\omega_{ce}}{\omega}$, i.e. low frequencies at a given B-field, also facilitate the plasma build-up after rf break down. Figure 1 shows that preionization is required up to a density such that $\omega_{pe} > \omega$ before the waves can take over. This is most likely to be achieved in low pressure gas by secondary electron

resonance breakdown [10]. The breakdown fields are then at a minimum between 10 and 100 MHz and increase sharply for higher frequencies.

The present results are ordered in the following way. After a description of the apparatus in Sec. II, the overall rf plasma properties obtained in the frequency range 35 to 200 MHz are given in Sec. III: density and temperature profiles, their pressure and power dependence and the influence of the rotational transform t . In Sec. IV we identify the role of the electron plasma waves in ionization and heating of the plasma. Of crucial importance is the occurrence of the resonance cones which emanate from our finite length source. The very existence of these resonance cones enhances the possibility of parametric decay, which is found to guarantee the efficient absorption mentioned before. A description of the parametric effects observed and the ensuing ion heating is given in Sec. V.

As far as the source efficiency is concerned, one can distinguish two regimes of operation: an ionization regime and a heating phase. During the ionization phase, the powerwise extent of which increases with increasing frequency, the source efficiency amounts to 35 %, or more if some electron conductivity anomaly is considered. In the heating regime, the propagation characteristics of the resonance cones together with the parametric absorption length provide a build-in saturation mechanism which impairs the efficiency for increasing powers. These aspects are mainly discussed in Sec. VI.

The Appendices discuss the observed decay phenomena in the light of the existing theory. Appendix A deals with thresholds, growth rates and absorption lengths. Appendix B discusses the possible influence of convection in view of the non-uniformity of the pump.

II. Description of the Apparatus

The Wendelstein II a (W II a) stellarator (Fig.2) has a major radius of $R = 50$ cm and a minor radius of $r = 9$ cm. A constriction at the section where the two half-torus parts join together reduces the effective tube radius to about 6 cm. The toroidal magnetic field B_0 is varied up to 6 kG and the rotational transform $t = \frac{1}{q} = \frac{R}{r} \frac{B_{pol}}{B_0}$ is mostly in the range $0 \lesssim t \lesssim 0.2$. The working gas is H_2 at pressures of $5 \cdot 10^{-6}$ to $3 \cdot 10^{-4}$ torr. The radiofrequency power ($35 \text{ MHz} \leq f \leq 200 \text{ MHz}$) is coupled into the stellarator via one or two electrostatic ring-shaped electrodes 10 cm in diameter, 4 cm wide and 10 cm apart, which at the same time serve as a limiter. The distance of the couplers to the torus wall is about 4 cm. As our main objective is the elucidation of the wave-plasma interaction, we choose to work in a steady state plasma obtained by injecting up to 300 W cw.

Figure 2 shows a sketch of the experimental set-up and the relative location of the various diagnostic instruments applied. Radially movable Langmuir and coaxial rf probes were applied to measure the local plasma density and electron temperature. Ion temperatures were derived from both an electrostatic analyzer measuring $T_{i \parallel}$ in the plasma column edge region and the Doppler broadening of a Ba ion impurity line. Further diagnostics include diamagnetic measurements and 4 mm interferometry.

No systematic study was made of the plasma breakdown phase. In the gas pressure and frequency ranges investigated the incident power P_i , required to start the discharge, ranges from 30 W to 200 W with the expected frequency dependence. The density rise time is typically 100 μsec to 200 μsec . After breakdown, the plasma can be maintained with power levels as low as 1 W. The coupling efficiency $\frac{P_i - P_r}{P_i} = \frac{P}{P_i}$, where P_r stands for the reflected and P for the total absorbed power, ranges from 70 % at 35 MHz to more than 95 % between 100 MHz and 200 MHz. Therefore, and as the generator supports the reflection prior to firing, no matching network is required. These results confirm the excellent coupling efficiencies previously reported in lower hybrid experiments [11] and predicted theoretically [12].

III. Overall Plasma Properties

With increasing power at fixed frequency, the line density as observed through the plasma center $\int N_e dr$ varies as shown in Fig.3. Radially resolved measurements of the ion-saturation current to the Langmuir probe (see, for example, Fig.4) show a parabolic density profile during the initial linear portion of the $(\int N_e dr, P)$ curve in Fig.3. Where the line density starts to level off, with growing power, the peak density stops rising and the profile only widens and tries to fill the whole volume delimited by the launching structure.

At low applied frequencies, this saturation density corresponds to the lower hybrid density (see Fig.3) in accordance with the scheme put forward in the introduction. The quantitative interpretation of ion-saturation measurements is somewhat shaky owing to the plasma rf signal and plasma temperature both varying strongly with the rf power and frequency (see below) and so influencing the measured probe current. It is then difficult to ascertain how closely the lower hybrid density can be approached, or even whether it could be exceeded. It should also be noted that the density obtainable for a given rf power at fixed frequency strongly depends on the gas pressure. The plasma density generally decreases with growing gas pressure probably as a result of a reduction in confinement time. The best measurements were therefore obtained at a low pressure around $1 \cdot 10^{-5}$ torr.

At higher frequencies, the corresponding lower hybrid density could not be reached since profile broadening sets in before this density limit is reached with growing rf power (Fig.3). This is observed in connection with sudden density profile rearrangements which occur at a rf power which also depends on the rotational transform t . It should be stressed that this density redistribution hardly shows up interferometrically. This behaviour is illustrated in Fig.5. Here the local density variation as a function of the rotational transform is shown, as measured at 3 radial positions ($r = -2, 0, +2.5$ cm) of a Langmuir probe and at fixed rf power and frequency. Also shown in this figure is the corresponding interferometer reading. For low values of t , the profile is

about parabolic; at $t \approx 0.11$ it goes over rather suddenly into a square-shaped one, although unnoticed by the interferometer. This phenomenon does not occur at rational values of t at which in another experiment [13] severe pump-outs have been observed. Under our experimental conditions pump-outs at rational t values could also be observed, but only under very low pressure conditions and at reduced toroidal B-field. Otherwise, the rational t values manifest themselves in a way not unlike the above reported evens: a mild modulation of the global density, with density increases at some radial positions and decreases at others, is observed.

The electron temperature profiles are closely related to the density profiles. At low power levels, both the density and T_e -profiles are parabolic. As the density distribution tends to broaden with increasing power, the electron temperature profile firstly flattens and then a strong non-uniformity develops with finally a marked temperature drop in the plasma centre and peak temperatures in the outer plasma column region. Such a power sequence of radial temperature distributions under somewhat extreme conditions is shown in Fig. 6 for $f_0 = 35$ MHz. This figure also gives some indication of typical temperature values recorded. At fixed power, parabolic profiles are more likely to be found at higher frequencies as exemplified in Fig. 7. The temperature non-uniformity is most pronounced near the coupler and, as one may expect, some smearing out occurs with increasing axial distance from the coupler. However, the radial position of the temperature maximum does not vary along the torus, as seen in Fig. 8. From Fig. 6 it is clear that while the electrons are undoubtedly heated with increasing power, the efficiency drops as the plasma heating preferentially occurs closer to the plasma edge, this giving rise to ever increasing temperature gradients. In Ref. 8 the electron temperature was reported to be power-independent, which was traced back to the particular expressions for the balance between the ionization rate and the rate of end losses. In our case the diffusion occurs, of course, radially and presumably follows quite a different although unknown temperature dependence. Globally, owing to the subtle interplay of heating and losses the average temperature

only mildly increases with rf power. One should also note that the mere decrease of energy deposition in the centre is not sufficient to explain the observed temperature minimum. We come back to this point in the next section after identifying the cause of the observed lack of energy penetration.

Measurements of the ion temperature over the whole plasma diameter proved to be impossible. The difficulty stems from the impossibility of introducing the electrostatic analyzer beyond the outer plasma edge without (i) disturbing the overall plasma behaviour by gross plasma losses on the analyzer surface and (ii) electron emission at the analyzer grids due to heating up effects. Owing to the small openings of the viewing ports of the W II A stellarator the Ba spectroscopy [30], on the other hand, gave data only in the vicinity of the plasma centre, with no overlapping region by the electrostatic analyzer method. Figure 9 gives results of such measurements of T_i derived from analyzer data together with T_e -values obtained from Langmuir probe characteristics. The Doppler broadening measurements of a Ba^+ line indicate a barium ion temperature distribution which corresponds to that of the electron temperature. It should be remarked that the H^+ temperature may be still higher than the measured Ba^+ temperature, because the ion energy exchange time between Ba ions and protons is comparable with or longer than the plasma confinement time. On the other hand, direct heating of the Ba ions by the rf power cannot be completely ruled out. Therefore, it cannot be said that the Ba^+ temperature distribution is an exact replica of the proton one. This remark is at variance with a previous interpretation in Ref. 14. It is important to note that both the analyzer and the Doppler broadening data indicate ion heating of the body of the velocity distribution function.

Of great importance for the interpretation of the above plasma behaviour are the confinement characteristics of the stellarator. The particle confinement time could be deduced from the density decay in the afterglow phase of a pulsed discharge.

It turns out that

- (i) τ_p only slightly changes with the electron density (varied with the applied frequency).
- (ii) τ_p is smaller for squared density profiles as compared with parabolic ones (compare FM 1 results [15]).
- (iii) practically all τ_p values are found to correspond to $[(0.5 \dots 1) n_o < \sigma v >]^{-1}$, where n_o is the neutral particle density corresponding to the filling pressure, σ is the ionization cross-section and $< >$ denotes an average over the distribution function having a mean temperature corresponding to the measured one (averaged over the radius).

The actual values range from about 400 μsec at hydrogen filling pressure of $p = 5 \cdot 10^{-5}$ torr to about 1200 μsec at $p = 8 \cdot 10^{-6}$ torr. The neutral particles are therefore practically uniformly distributed over the whole torus and the processes of ionization, radiation and elastic energy exchange of the H^+ ions are uniformly distributed over the entire plasma volume.

For the further discussion, it is also relevant to point to the following ordering of the various collision times $\tau_{\alpha\beta}$, which are valid over the entire parameter range covered:

$$[5 \cdot 10^{10} \text{ cm}^{-3} \leq n_e \leq 7 \cdot 10^{11} \text{ cm}^{-3}, 6 \text{ eV} \leq T_e \leq 15 \text{ eV}, 1 \leq T_i \leq 10 \text{ eV}] :$$

$$\tau_{i',i} \ll \tau_p \sim \tau_{i,n} < \tau_{e,i} \ll \tau_{i, Ba^+}.$$

IV. Interdependence of Resonance Cone, Density and Temperature Profiles

The dramatic levelling off of the density at a value close to the lower hybrid density corresponding to the applied frequency provides an important clue to the role played by the electron plasma waves in sustaining the plasma. It is, however, well known [9] that the dispersion of the electron waves is such that the energy emanating

from a finite rf source is localized along well-defined surfaces, the resonance cones, which have an angle with the magnetic axis of

$$\psi = \tan^{-1} \left[\left(\omega^2 - \omega_{LH}^2 \right) \cdot \left(1 + \frac{\omega_{pe}^2}{\omega_{ce}^2} \right) / \left(\omega_{pe}^2 - \omega^2 \right) \right]^{1/2}. \quad (2)$$

In Ref. 16 we reported on the kinematic aspects of the cone propagation and on some detailed comparison of the fine structure of the rf fields inside the cone with theoretical calculations by Bellan and Porkolab [17]. Equation (2) predicts that the closer the density approaches the critical lower hybrid density, the longer will be the path the energy will have to travel to reach the plasma centre.

This behaviour is illustrated in Fig. 10, where we plot at a given toroidal distance from the source and as a function of rf power and for different frequencies the radial position up to which the cones were able to penetrate the plasma column. At a fixed power, the cones can move further radially inwards with increasing frequency. This is consistent with the observation that very few watts are needed to reach the limiting density at low frequency. In Fig. 10, the measured radial displacements are furthermore compared with those found from integration of Eq. (2) from the coupler position up to the observation plane using the particular density profile pertaining to each experimental condition. The same theoretical calculations predict that an energy packet leaving the rf structure would eventually reach the centre (i.e. they travel 5 cm inwards) after passing along the plasma column about 2 m through a square plasma profile with a density equal to 50 % of the lower hybrid density and after passing some 5 m when the density attains 90 % of this density limit.

Hence, although the formation of the resonance cones constitutes an extreme localization of the energy (and possibly of its deposition), the energy will still be able to pervade the whole plasma column provided the lower hybrid is nowhere present in the density profile and provided the absorption length is longer than a few metres. Therefore, it is extremely important to note that the electron temperature profiles show a strong non-uniformity even under conditions when the maximum density remains well below the lower hybrid density. The collisional

damping length for electron plasma waves is approximately given by

$$L_c \approx \frac{1}{\text{Im } k_z} \approx \frac{2\omega}{\nu_e (\text{Re } k_z)}, \text{ where } \nu_e \text{ is the collision frequency of electrons}$$

with ions and neutrals. Under our experimental conditions ν_e ranges from 0.2 to 1 MHz. We then further assume that the lowest (i.e. least damped) component of the k_z -spectrum, which through interference generates the cones, is given by the lowest eigenmode or Trivelpiece-Gould mode [19] of the plasma column, and that the main body of the spectrum does not extend beyond the twentieth eigenmode [19, 20]. L_c is then of order $(0.1 \dots 4) 10^{-2} \omega_{pe} \nu_e^{-1}$ metre, i.e. 100 to 1000 m at $N = 10^{11} \text{ cm}^{-3}$. Landau damping would yield absorption lengths L_ℓ of the order $L_\ell = \pi^{-1/2} \xi_0^{-3} \exp(\xi_0^2) (\text{Re } k_z)^{-1}$, where $\xi_0 = \omega/k_z V_{the}$.

On the same assumptions as before, L_ℓ would be even higher than L_c .

The experimental absorption lengths appear to be one or two orders of magnitude smaller than either L_c or L_ℓ . Quantitatively, one requires effective collision frequencies of the order of the ion plasma frequency (see also Appendix A) to understand the experimental absorption length.

A more adequate explanation for the temperature non-uniformity (see Figs. 6,7,8) seems to be the observed parametric decay of the electron plasma wave into another electron plasma wave and an ion wave with a frequency slightly above the ion cyclotron frequency (see Sec. V). Both decay waves could be a priori responsible for the electron heating and it is reassuring that both have a spatial distribution which is like the resonance cone of the fundamental electron waves as shown in, for instance, Fig. 11 and must therefore lead to "localized heat deposition".

In Appendix B we discuss in more detail this localization of the decay waves with regard to the pump inhomogeneity. We should also point out that the phenomena studied here are different from those described in Ref. 21, where surface waves provided a similar edge heating effect under the condition $\omega_{pe} > \omega_{ce}$. Under our experimental conditions ω_{pe} was always smaller than ω_{ce} .

In a toroidal device, of course, localized heat deposition near the plasma edge as induced by resonance cones is not sufficient to explain the observed profiles. Unlike in a linear machine, the energy balance has to be mainly radial and we therefore consider the radial heat balance equation:

$$-\nabla_{\perp} (\chi_e \cdot \nabla_{\perp} T_e) = Q_s - Q_L \quad (3)$$

where χ_e is the electron conductivity, Q_s is the heat production and Q_L the heat loss term excluding conduction losses. The curvature of the temperature profile is negative where $Q_s - Q_L$ is positive, i.e. where the resonance cones have dumped the major part of the energy. However, for the curvature to change sign, the local heat loss must more than outweigh the power input. As the cone location, its appearance and the ensuing profiles gradually change along the axis, any such bookkeeping can only be approximate. The ionization plus radiation losses per unit volume Q_{IR} amount, according to Ref. 22, to $(NK \cdot 24 \text{ eV}) \tau_p^{-1}$ for ionization from H or H_2 . Heating of the newly formed particles amounts to $\frac{3}{2} NKT_e \tau_p^{-1}$ and electron losses to the ions require $Q_{ei} = 1.3 \cdot 10^{-26} \alpha N^2 T_i^{-1/2} \text{ watt} \cdot \text{cm}^{-3}$, where α is a very weak function of T_e/T_i with a mean value of 0.33 for $1.5 < T_e/T_i < 10$. For a typical case of $p = 3 \cdot 10^{-5}$ torr, $N = 1.5 \cdot 10^{11} \text{ cm}^{-3}$, $T_e = 10 \text{ eV}$, $T_i = 4 \text{ eV}$, Q_i adds up to about $2.0 \cdot 10^{-3} \text{ Wcm}^{-3}$. This figure is, of course, much less than the total injected energy averaged over the total plasma volume (typically 10^{-2} Wcm^{-3}) and without resonance cones, the temperature profiles would always be a parabolic one. However, radial rf potential distributions for the sideband waves with averaged amplitude ratio of 1:3 or 1:4, i.e. energy ratio of 1:9 or 1:16 between cone maximum and plasma centre, are not unusual and are certainly sufficient to explain the change of curvature.

In summary, it is clear that the temperature profiles point to an energy deposition which, with increasing power, occurs more and more near the plasma edge. The resonance cone properties are instrumental in bringing this about, although neither collisional nor electron Landau damping can explain the required damping length. Obviously, the detrimental interdependence of power increase, profile

widening and cone behaviour might be interrupted in a fully ionized plasma. Such conditions can only be achieved for the higher frequencies and at pressures below $1.0 \cdot 10^{-5}$ torr. Unfortunately, the mean lifetime of our rf probes becomes prohibitively short under these circumstances to allow the usual steady state diagnostics.

V. Parametric Effects And Ion Heating

While looking for an explanation for the presumed very short absorption lengths, we ought also to account for the high ion temperature measured. The electron-ion energy equilibration immediately comes to mind as ion heating process. Equating Q_{ei} , given above, to the most optimistic loss rate by assuming an energy loss at the particle diffusion rate, one finds, for $\tau_p = 500 \mu\text{sec}$, $T_i \approx 10^{-11} \text{ N}$. For densities as low as $4 \cdot 10^{10} \text{ cm}^{-3}$ as in Fig. 9, T_i is expected to be at most 0.6 eV. Ion temperatures ten times higher than calculated from equipartition are not unusual in our case. Furthermore, Fig. 9 also illustrates another shortcoming of equilibration in explaining the ion heating. At the low frequency at hand ($f = 35 \text{ MHz}$), the density is independent of the power level. Hence, the only way in which the absorbed power could influence Q_{ei} is via T_e and, therefore, very little power dependence should be seen. Wave heating appears to be an adequate supplement for the equilibration heating. Ion heating might come about by Landau damping of the ion waves into which the lower hybrid waves can convert linearly [23] before actually reaching the hybrid density N_{LH} . The density N_c where mode conversion occurs is roughly given by $N_c = N_{LH} \left[1 - 0 \left(\frac{k_z V_{the}}{\omega_{LH}} \right) \right]$,

where $T_i \leq T_e$. For experimentally significant k_z values the conversion density is so close to the lower hybrid density, that not reaching the latter density amounts to excluding mode conversion.

The experimental evidence points to parametric decay as the primary ion-heating mechanism.

(i) Typical decay spectra can be seen in Fig. 12. Shown here are sideband spectra around a pump frequency of 200 MHz for various toroidal magnetic fields. The low frequency component (not shown) occurs at the difference frequency $f_\ell = f_o - f_s$ in accordance with the selection rules. One can verify that f_ℓ varies proportionally with the magnetic field with an absolute value somewhat higher than the ion-cyclotron frequency ($f_\ell: (1.05 \text{ to } 1.1) f_{ci}$). Direct experimental checks of the wave dispersion proved to be impossible owing to the pump inhomogeneity and the difficulty in measuring axial wavelengths in a toroidal machine, especially in a stellarator with very limited access. In view of the value of f_ℓ at least two interpretations, namely electrostatic ion-cyclotron wave decay or quasi-mode decay, are possible. Both alternatives are discussed in detail in Appendix A.

(ii) Distinct thresholds are observed at power levels as low as 10 W. Figure 13 shows the amplitude of the low-frequency decay component of the instability as a function of the applied power measured at various gas filling pressures for $f_o = 200$ MHz. The threshold power increases less than proportionally with the background pressure.

(iii) Proportionality between the measured potentials of the low (ϕ_ℓ) and high (ϕ_s) frequency instability components is observed as shown in Fig. 14. This proportionality prevails on the average over most of the radial extent of the waves. For the example shown, all field amplitudes were measured in the plasma centre and at a distance of about 60 cm from the coupler.

The fact that there is no dependence on the pump amplitude can be explained by assuming that the power absorbed in both components is given by the growth rate γ_o times the respective energy densities. (In reality this argument would only apply for the saturated, integrated spectrum, not for its maximum.)

The Manley-Rowe relation [23] then requires these power densities and,

hence, the energy densities to be proportional to the frequency ratio f_s / f_ℓ . This then imposes a relation between the potentials in which the pump amplitude does not intervene.

One will notice that there is a systematic deviation from linearity at the lowest power levels. We attribute this to the change in particle density which, as shown in Fig.3, is typical of these power levels. Such a change in density could, for instance, cause the observed shift when ϕ_ℓ pertains to an electrostatic ion-cyclotron wave. The energy density is then essentially given according to [24] by

$$W_\ell = \frac{\omega_{pi}^2 \omega_\ell^2}{(\omega_{ci}^2 - \omega_\ell^2)^2} \cdot \frac{k_{\perp\ell}^2 \phi_\ell^2}{8\pi}, \quad (4)$$

whereas

$$W_s = \frac{\phi_s^2}{16\pi} \left[\frac{k_z^2 \omega_{pe}^2}{\omega_s^2} + k_{\perp s}^2 \right]. \quad (5)$$

As ω_ℓ (and hence $k_{\perp\ell}$) is practically constant and $\omega_s \simeq \omega_0$ is close to or proportional to ω_{pi} , W_ℓ is proportional to N and ϕ_ℓ^2 , whereas W_s has hardly any density dependence. As, furthermore, it holds that

$$W_\ell \sim \frac{f_\ell}{f_s} \cdot W_s, \text{ one then derives the following scaling:}$$

$$\frac{\phi_\ell^2}{\phi_s^2} \sim \frac{f_{ci}}{f_0} \cdot \frac{1}{N}. \quad (6)$$

This expression also renders plausible the enhancement of the sideband amplitude at increasing pump frequency f_0 . Both f_0 and N increase when passing from 50 to 110 MHz. Of course, more quantitative comparisons can only be made in the framework of a more specific theoretical model.

- (iv) The ion heating is closely correlated to the intensity of the instability as seen in Fig. 15 and 16. In both cases the correlation is made with the sideband since it is the largest and, therefore, easier to measure accurately.

In Fig. 15 we plot as a function of power, on the one hand, the integral over the plasma radius of the amplitude squared of the sideband potential ($f_s = 42$ MHz) and, on the other hand, the temperature increase ΔT_i with respect to the value existing before the instability onset measured by the electrostatic analyzer at a radius of 4 and 3 cm from the plasma centre.

In Fig. 16 the fields are local values measured in the plasma centre for $f_o = 50$ MHz and 110 MHz, and T_i is obtained at $r = 3.5$ cm. The extrapolation towards zero field gives temperatures T_{io} of about 1 eV, as might be expected from equipartition for $\tau_p \approx 700 \mu\text{sec}$ ($p = 2 \times 10^{-5}$ torr) and $n = 6 \times 10^{10} \text{ cm}^{-3}$ and $1.5 \times 10^{11} \text{ cm}^{-3}$. The experimental points were fitted (at $\phi_s = 0$ and $\phi_s = 10$ for $f_o = 50$ MHz) by a quadratic dependence on ϕ . This rather intuitive dependence can be corroborated by the following simplifying arguments. We expect ΔT_i to obey (see Sec. VI):

$$\frac{3}{2} \cdot NK \cdot \Delta T_i = \alpha \gamma_o \cdot W_\ell \cdot \tau_i^{-1} \quad (7)$$

where α denotes that fraction of the energy of the low-frequency component that goes into ion heating and τ_i is the ion confinement time which in first approximation equals τ_p and is therefore essentially only pressure dependent. Using (4), (6) and the expression for γ_o given in Appendix A ($\gamma_o \sim f_o^{1/2} \cdot \frac{U}{V_s}$) one finds

$$\Delta T_i \sim \alpha \phi_s^2 \cdot f_o^{-1/2} \cdot N^{-1} \cdot \frac{U}{V_s} \quad (8)$$

Furthermore, we find experimentally that $\frac{U}{V_s}$, the ratio of the pump induced electron drift to the ion sound speed, changes by typically 20 % for a corresponding change of 200 % in ϕ_s . The curve for $f_o = 110$ MHz is only fitted at T_{io} and further obtained by dividing the ΔT_i at 50 MHz by 3.75, which is the value suggested by Eq. (8) as far as the contribution from f_o and N is concerned.

The greatest unknown is α since it involves among other things a knowledge of the (non-linear) interaction inside the instability spectrum. In practice, α and not ΔT_i will be the result of Eq. (8) and whatever quantitative agreement could be deduced from comparisons such as in Fig. 16 is always bound to be somewhat fortuitous. This matter is further discussed in Sec. VI.

Some important questions remain unanswered. The nature of the low-frequency waves was not investigated in detail and therefore the mechanism for ion heating remains unclear. This is also partly due to a lack of guidance from the existing theoretical models, which under our experimental conditions lead to overlapping predictions for some of the most direct experimental checks, as discussed in Appendix A.

VI. Some Remarks on Efficiency

The electron energy balance was already briefly touched upon in Sec. VI in connection with the radial electron temperature distribution. Here we discuss the overall source efficiency and the ion energy balance.

Figure 17 shows the $N(T_e + T_i)$ values found from the diamagnetism for four frequencies at $P = 300$ W. The corresponding source efficiencies η are obtained from the following relation:

$$\eta \cdot P = (Q_H + Q_{IR} + Q_{i,n}) V + \int_s K (\alpha_e \cdot \nabla T_e + \alpha_i \cdot \nabla T_i) dS \quad (9)$$

Q_H here is equal to $\frac{3}{2} \cdot NK(T_e + T_i)$, Q_{IR} is the ionization and radiation loss defined before, and $Q_{i,n}$ represents the ion losses to the neutrals, being estimated at $\frac{3}{2} \cdot \frac{NKT_i}{2} \cdot \frac{1}{\tau_p} \cdot \frac{\langle \sigma v \rangle_{ec}}{\langle \sigma v \rangle_{ion}}$, where the ion-neutral elastic collision cross-section times the ion velocity averages to an almost constant value of $8.75 \cdot 10^{-9} \text{ cm}^3 \text{ s}^{-1}$, i.e. practically equal to the ionization - $\langle \sigma v \rangle_{ion}$

for the electron temperature range 10 to 15 eV. The integral in Eq. (9) has to be taken over the toroidal plasma surface. The ion mean free path λ_{ii} is about equal to the connection length R/ℓ . As such, the ion conductivity scaling is ambiguous, although the absolute value is rather well known. Rather than conjecture any anomalous electron loss, we drop the electron conductivity term in Eq. (9). This results in source efficiencies which are then, possibly even severe, underestimations.

As an illustrative example we consider the 200 MHz case of Fig. 17 with $\tau_p = 700 \mu\text{sec}$ ($p = 1.25 \times 10^{-5}$ torr), $V = 13 \ell$ and $\nabla T_i = T_i / a$. One then finds $Q_H V = 26 \text{ W}$, $Q_{IR} V = 23.5 \text{ W}$, $Q_{i,n} V = 3.5 \text{ W}$ and the ion conductivity losses amount to 4.2 W, yielding a total efficiency $\eta = 19 \%$. By far the largest power investment has to be made in the ionization on the one hand and the heating of the newly created particles on the other. From Fig. 3 we know that ionizing most of the particles requires rather low power (15 W at 50 MHz, 100 W at 200 MHz): this is the phase of the almost linear (N, P) curves and the parabolic density profiles. In the saturation regime (on the right side) of the same curves a power increment will increasingly be hampered by the decreasing penetration of the resonance cones. Figure 17 can then be easily understood. Working at high frequencies results in a favouring of ionization over heating, i.e. a prolongation of the linear (N, P) characteristic. This is the most efficient process and efficiencies along this line amount to an optimum of about 35 %. Moving away from this regime in the (N, P) plane means decreasing the efficiency: the farther away, the worse is the efficiency. As such, η drops from 35 % at 15 W to 3.5 % at 300 W for $f_0 = 50 \text{ MHz}$. Although the generator does not allow operation beyond 200 MHz, we also expect the efficiency to level off at higher frequencies at the above optimal value.

We therefore conclude that the resonance cones act as a built-in saturation mechanism. Because of this, the efficiency is satisfactory up to an optimal amount of power corresponding to that necessary for bringing the source up to the end of the ionization regime. Applying more power will still result in an increased energy content, but at a reduced efficiency.

Two reasons prompt us to investigate the ion energy balance in some detail. Firstly, the ions are usually found to diffuse in a classical fashion, i.e. without invoking the need for anomalous processes and allowing some straightforward bookkeeping of power input and output. Secondly, we want to check to what extent it is possible to transfer wave energy directly to the ions without relying on electron heating and subsequent equipartition.

The global ion efficiency is defined as $\eta_i = \frac{P_{ion}}{P}$, where the ion losses P_{ion} add up to

$$P_{ion} \approx \frac{3}{2} \cdot \frac{NKT_i V}{\tau_p} + Q_{i,n} V + \int_S K \chi_i \cdot \nabla T_i \, dS, \quad (10)$$

which should be balanced against the power input from equipartition ($Q_{ei} V$) and wave heating. The conductivity losses are estimated to equal $2.1 \cdot 10^{-23} T_i^{1/2} N^2$ watt for Pfirsch-Schlüter losses and $7 \cdot 10^{-14} T_i^{5/2} N$ watt for plateau losses, where T_i is expressed in eV and N in cm^{-3} , assuming $\nabla T_i \approx T_i / a$. Pump frequencies close to the lower hybrid frequency are often advocated for parametric heating by the argument that the Manley-Rowe relation in that case guarantees the highest possible power input P_ℓ in the low-frequency decay component, which is the most natural candidate for interaction with the ions. P_ℓ is then equated to $\frac{f_\ell}{f_o} \cdot (P - P_{thr})$. The power at threshold P_{thr} is introduced in order to account in the total wave power in some approximate way for the pump dissipation. As such

$$P = P_{thr} + \frac{f_s}{f_o} (P - P_{thr}) + \frac{f_\ell}{f_o} (P - P_{thr})$$

Of course, P_ℓ can equally well heat the electrons, and the Manley-Rowe power ratio should be seen as a statement of the maximum of what might go to the ions. On this assumption one might define an alternative efficiency α such that αP_ℓ is that part of the wave energy which is really fed into the ions. (See also Sec. V, iv). Figure 18 shows an example of an instance where α turns out to be practically equal to one. For $f_o = 200$ MHz, $p = 1.0 \cdot 10^{-5}$ torr,

we plot the observed mean ion temperature, corresponding to the profiles shown in the inset, as a function of power. In view of the difficulty in scanning the whole profile, the values at $r = 2$ cm are taken as the average temperature. The lines are obtained by solving Eq. (10) where $P_{ion} = \alpha P_{\ell} + Q_{ei}V$ assuming either plateau or Pfirsch-Schlüter losses and posing $\alpha = 1$. Further we have $\tau_p = 900 \mu s$, $NV = 2.4 \times 10^{15}$ at $P = 100$ W, $3.6 \cdot 10^{15}$ at 200 W and $4.0 \cdot 10^{15}$ at 300 W. We also assume $\langle \sigma_v \rangle_{ec} = \langle \sigma_v \rangle_{ion}$. The global efficiency η_i in these cases amounts to 5 %. Of the 10 W going to the ions at $P = 200$ W, only 2.3 W comes from the electrons via equipartition and 7.7 W comes from wave heating. To complete the balance: the conductivity losses account for some 4 W, the ion neutral collisions for 2.5 W and the particle losses for 3.5 W.

One sees that $\alpha = 1$ appears to be a good approximation over the entire power range. From this one would be tempted to infer that no anomalous ion energy losses are present and that consequently the rf fields do not have an adverse effect on the ion confinement. This conclusion can, however, not be fully corroborated experimentally as one cannot rule out a priori the possibility that the underlying balance is incomplete: some ion heating might, after all, come from the high-frequency component of the instability. In Table I we also list a series of runs at lower frequencies where the observed T_i is used to compute α and from which it would appear that the latter decreases with decreasing frequency. It is, however, impossible to ascertain whether a conductivity anomaly is present or whether simply a larger fraction of the wave energy is going to the electrons. The overall ion efficiency η_i decreases from some 5 % at 200 MHz to about 3 % at 35 MHz. These efficiencies are practically the same as those reported in [8] at $f_o = 144$ MHz. This general trend contradicts the a priori expectation that lower frequencies are favourable for ion heating because of the Manley-Rowe relation on the one hand and the lower

$$\frac{\omega_o - \omega_{LH}}{\omega_{LH}} \text{ ratio on the other.}$$

In conclusion, one can state that both the global source efficiency and the ion heating efficiency turn out to be quite favourable for the highest frequencies investigated ($f_0 = 200$ MHz). A built-in saturation comes about at high power as a result of the propagation characteristics of the resonance cones along which the wave energy pervades the plasma volume. The coupling proves to be excellent at all frequencies studied, although matching problems can be expected at those frequencies for which the vacuum wavelength is of the same order as or smaller than the structure dimensions. As a possible drawback of the higher frequencies we wish to mention their increased breakdown requirements.

Acknowledgements

We thank E.Hinnov and H.Ringler for the performances of the spectroscopic measurements, P.Böhm and many members of the technical staff of the stellarator division, and Ms.Weikmann for typing the manuscript.

APPENDIX A

Relation of the experiment to existing theory

Published theory on lower-hybrid wave decay in homogeneous plasmas is rather diverse and divergent and awaits selection through experimental confirmation. Two main categories are in competition: on the one hand, those invoking electrostatic ion-cyclotron waves [25,26] and, on the other, those involving quasi-modes or beat waves at $\omega_o - \omega_s = (\bar{k}_o - \bar{k}_{sz}) \cdot \bar{V}_{the}$ [27,28]. We find that for our experimental parameters the predictions of both theories on some of the most relevant experimental checks such as thresholds and growth rates seem to overlap more or less. We review some of these for the particular conditions pertaining to Fig. 11.

- (i) The electrostatic ion-cyclotron wave (EICW) occurs when $\omega_\ell \ll k_{z,\ell} V_{the}$ and obeys the dispersion relation $\omega^2 = \omega_{ci}^2 + k_\perp^2 V_s^2$, where V_s is the ion-acoustic velocity. When $\omega_{LH} < \omega_o < 3 \omega_{LH}$, decay of an electron plasma wave with the occurrence of an EICW can only be described by relaxing the dipole approximation [26], customary among theoreticians. Given the plasma parameters and the observed frequencies, the dispersion relations provide $|k_\perp|$ and the angles of propagation of the two electron waves with respect to the magnetic field (along the z-axis). Assuming then that the two decay waves lie in the plane (\bar{k}_o, \bar{z}) (the problem is then essentially two-dimensional) and invoking the selection rules, one finds that $\omega_\ell \ll k_{z,\ell} V_{the}$ can be verified for the two geometrical configurations in Fig. 19 (see also Ref.25). In case (a) one has $k_{z,o} \approx k_{z,s} > k_{z,\ell}$ and $k_{\perp,o} \approx k_{\perp,s} \approx k_{\perp,\ell}$, whereas in case (b) $k_{z,o} \approx k_{z,s} \approx \frac{k_{z,\ell}}{2}$ and $k_{\perp,o} \approx k_{\perp,s} \approx k_{\perp,\ell}$. In the former case the resulting $k_{\perp,o}$ seems to conflict with the theoretical picture of the resonance cones being a superposition of a limited number of Trivelpiece-Gould eigenmodes [19,20], thus leaving us with case (b)

as the most probable configuration. However, the growth rate for this interaction is quite low, and it has been shown [25] that far higher rates occur when $k_{\perp,s}$ is perpendicular to the (k_o, z) - plane. With this assumption, we find, however, that the geometrical and dispersion constraints, for the experimental conditions at hand, can only be satisfied for $k_{z,l} \approx \frac{\omega_l}{V_{the}}$. The instability, therefore, can only grow at a rate intermediate between the two-dimensional and the perpendicular cases. Using the expression for the growth rate without damping given in Ref.25

$$\gamma_o' = \frac{k_{\perp,l} V_s^2}{4 V_{the}} \sqrt{\frac{\omega_s}{\omega_l}} \left| \frac{e E_{z,o}}{m_e \omega_o V_s} + i \frac{\omega_{pe}}{\omega_o} \sin \psi \frac{U}{V_s} \right| \quad (A 1)$$

where ψ is the angle of $\vec{k}_{\perp,s}$ with the (k_o, z) plane, we then arrive at

$$\gamma_o' \approx 0.01 \cdot \omega_{pi} \cdot \frac{U}{V_s}.$$

Here, we used $\omega_l \approx 1.05 \omega_{ci}$, $T_e = 10$ eV, $f_o = 110$ MHz, $f_{ci} = 7.6$ MHz, $N = 1.5 \cdot 10^{11} \text{ cm}^{-3}$ and $\sin \psi = \frac{1}{2}$.

The linear damping rates for $\frac{\omega_l}{k_{z,l} V_{the}} \approx 0.1$ turn out as follows.

The EICW has a damping rate γ_l which is partly due to electron Landau damping ($0.01 \omega_{ci}$) and partly due to ion-cyclotron damping (up to $0.04 \omega_{ci}$).

The sideband wave is exclusively damped by collisions ($\gamma_s \approx 7 \cdot 10^{-4} \omega_s$).

The threshold is then obtained at $\frac{U}{V_s} = 0.20$. The dependence of the threshold power on collision via γ_s is experimentally verified as seen in Fig. 20, where the values of P_{thr} were taken from Fig. 13 and the collision frequency ν_e was calculated as a function of the pressure p , according to:

$$\nu_e = \nu_{en} + \nu_{ei} = (6.3 \cdot 10^9 p + 2 \cdot 10^{-6} N) \text{ Herz},$$

where $N = 10^{11} \text{ cm}^{-3}$ at the lowest pressure and $N = 3 \cdot 10^{10} \text{ cm}^{-3}$ at a pressure of $p = 3 \cdot 10^{-4}$ torr.

- (ii) Making the dipole approximation, Prokolab [29] predicts for parameters which are typical of the present experiment ($f_o = 200$ MHz, $B = 5$ kG, $N = 3 \cdot 10^{11} \text{ cm}^{-3}$, $T_e = 10$ eV, $\nu_e / \omega_o = 10^{-4}$) the occurrence of quasimodes (identified by the customary check on the susceptibilities) in the experimental range about ω_{ci} for $k_{z,\ell} \cdot \lambda_{De} \leq 0.03$. In Fig. 21 we plot an example of the dependence of the computed growth rate on U/V_s . The solid line represents $\gamma_o = \gamma_o' - \gamma_{lin}$ as previously found for EICW. One can verify that both the growth rate and the threshold are comparable for both schemes, even if the theoretical analytically obtained growth rates for quasimodes predict a quadratic dependence on $\frac{U}{V_s}$. For this case as well a change in neutral pressure will only affect the linear damping of the sideband wave.

An important question which was not investigated experimentally is whether the turbulence level is high enough to explain the short absorption lengths deduced from the particular temperature profiles. This involves an experimental determination of γ_o and a careful measurement of the ratio of the energy density of the instability to that of the pump, each integrated over the whole spectrum. Neither of these was attempted. Calculating L_c of Sec. IV using an effective collision frequency ν_{eff} as given by Rogister [28] would yield more than adequate absorption lengths. His ν_{eff} is given by

$$\nu_{eff} \sim \frac{U^2}{V_s^2} \cdot \frac{\omega_{pi}^2}{\Delta\omega}, \text{ where } \Delta\omega \text{ is}$$

the spectral width of the instability. However, this is based, on the one hand, on an optimal growth rate which for $\frac{U}{V_s} = 1$ is perhaps ten times larger than the γ_o given before and, on the other hand, on an instability level which appears quite high. This problem certainly deserves further scrutiny, preferably under conditions where the heating waves are launched on a target plasma.

APPENDIX B

The pump inhomogeneity and its repercussion on the decay waves

A priori, one expects that the existence of the resonance cones, as a result of the concentration of energy density, enhances the possibility of parametric decay. It is not surprising either to find that these decay waves have a cone-like distribution with a maximum amplitude at the location of the pump-resonance cones. However, it might be argued that the instability, which is convective, might be carried outside of the nonuniform pump region in a time which is, at least for practically attainable field values, much shorter than the inverse growth rate. We, therefore, check whether the field strengths that allow the instability to grow are compatible with those to be expected in the experiment.

The geometry of the interaction is sketched in Fig.22. The (\bar{k}_o, \bar{z}) plane is chosen as (x, z) plane. An energy packet leaves the coupler with a group velocity $\bar{v}_{g,o}$ along a path making an angle ψ_o with the z -axis. The centre of the instability, which starts to grow at P , propagates at a speed and along a direction given by

$\frac{\bar{v}_{g,s} + \bar{v}_{g,l}}{2}$ [25], where $\bar{v}_{g,s}$ and $\bar{v}_{g,l}$ are the group velocities of the

sideband wave and the low-frequency decay waves respectively. As the sideband itself is an electron plasma wave with a frequency only slightly different from that of the pump, its group velocity lies on a resonance cone making an angle $\psi_s \approx \psi_o$ with the magnetic field. The exact position of $\bar{v}_{g,s}$ on this cone follows from the dispersion relation and the selection rules. $\bar{v}_{g,l}$ is usually of the order of the ion-acoustic speed and is much smaller than $\bar{v}_{g,s} \approx \frac{\omega_s}{k_{z,s}} \left(1 - \frac{\omega_{LH}^2}{\omega^2}\right)$.

When ω is not too close to ω_{LH} , this velocity exceeds the electron thermal velocity. The instability pulse therefore moves along the cone of the sideband wave and the angle χ between $\bar{v}_{g,s}$ and $\bar{v}_{g,o}$ is bounded by $\psi_o - \psi_s \leq \chi \leq \psi_o + \psi_s$. The discussion in Appendix A has shown that the exact orientation of \bar{k}_s (to which $\bar{v}_{g,s}$ is perpendicular) is not exactly known. We therefore simply assume that $\chi \approx \psi_o$.

Finally, the instability leaves the pump region after an approximate time

$$\frac{\delta}{v_{g,s} \sin \chi}, \text{ where we take for } \delta \text{ the experimental width of the pump}$$

field distribution (see Ref. 16 for a comparison of this width with theory).

For the experimental data pertaining to Fig. 11: $N = 1.6 \cdot 10^{11} \text{ cm}^{-3}$, $T_e = 10 \text{ eV}$, $f_o = 110 \text{ MHz}$, $f_s = 102 \text{ MHz}$, $f_l = 8 \text{ MHz}$, one finds $\gamma_o = 1.25^\circ$, $\gamma_s = 1^\circ$ and $\delta = 1.5 \text{ cm}$.

The convective threshold can be obtained by comparing $v_{g,s} \sin \chi \delta^{-1}$ to γ_o ,

which is given in Appendix A. The threshold thus calculated is expected to be

higher for quasimode decay than for EICW decay because of the difference in

$v_{g,s}$. For quasimodes in the dipole approximation, $v_{g,s} = \frac{\omega_s}{k_{z,s}} = \frac{\omega_s}{\omega_l} V_{\text{the}}$.

For EICW, $|k_{z,l}| \approx 2 |k_{z,s}|$ and $v_{g,s} = 2 \frac{\omega_s}{\omega_l} \cdot \frac{\omega_l}{k_{z,l}}$, where $\frac{\omega_l}{k_{z,l}} \ll V_{\text{the}}$.

For an interaction involving quasimodes one therefore expects much higher group

velocities. For $\chi = 1.25^\circ$, one finds $\frac{U}{V_s} \approx 0.15$ for EICW with

$\frac{\omega_l}{k_{z,l} V_{\text{the}}} = 0.1$ and $\frac{U}{V_s} = 0.75$ for quasimodes. The thresholds under the combined

influence of dissipation and convective then amount to $\frac{U}{V_s} \approx 0.4$ to 1.0 .

The absolute field intensities were not measured in the experiment. Very

approximate values can be calculated in the following manner. The observed

threshold power is typically some 10 W. Assuming perfect matching (in view of

the very low reflection coefficients), the voltage at the plates is then estimated

to be 22 V. At the plate-radius, $E_z = \left| \frac{d\phi}{dz} \right|$ is a J_0 -function. Between the plates

and the cut-off layer at $\omega = \omega_{pe}$ the singularity is smeared out because of the rapid decrease with distance of the high k_z components of the applied spectrum.

We expect E_z values at the cut-off layer of some 11 V/cm. According to the

W.K.B. calculations of Bellan et al. [17], the E_z values in the plasma are

essentially an image of the distribution at the boundary corrected from some

density variation which follows a $1/4$ power dependence. At the cone maximum

of Fig.11, we expect E_z to be some 2 V/cm and,

$$\text{as } E_{\perp} = E_z \cdot \left[k_{\perp}^2 - \left(1 - \frac{\omega_{pe}^2}{\omega^2} \right) \cdot \frac{\omega^2}{c^2} \right] / k_{\perp} k_z, \text{ one finds}$$

$E_{\perp} \approx 80$ V/cm and finally $U/V_s \approx 0.5$. These values are based on a calculation in plane geometry and some further increase due to cylindrical focusing should be taken into account.

This rough evaluation appears to guarantee that under our experimental conditions convection imposes thresholds comparable to those imposed by dissipation and which correspond to power levels which are plausible. The observed dependence of threshold on the electron collision frequency reported in Appendix A is an experimental proof of the predominance of the dissipative effects over the convective ones. This, in turn, might perhaps be used as an argument in favour of EICW decay.

An important implication of the above calculations appears to be the fact that convective damping alone is not enough to guarantee the propagation of the slow wave up to the lower hybrid conversion layer without parametric decay in lower hybrid fusion experiments. An extrapolation of our results, on the assumption that $\frac{U}{V_s}$ is the only scaling factor, would predict convective threshold powers of some 30 kW in a plasma of 1 keV and $B_0 = 30$ kG. Finally, it is thought that the possible wave number mismatch is not likely to alter these conclusions fundamentally.

R e f e r e n c e s

1. G. Lisitano, M. Fontanesi, and S. Bernabei, Phys. Rev. Letters 26, 747 (1971).
2. A. Aubert, A. M. Messiaen, and P. E. Vandenplas, Appl. Phys. Lett. 18, 63 (1971).
3. S. Bernabei, R. De Dionigi, and M. Fontanesi, Appl. Phys. Lett. 22, 85 (1973).
4. M. Porkolab, V. Arunasalam, and R. A. Ellis, Jr., Phys. Rev. Letters 29, 1438 (1972).
5. W. M. Hooke and S. Bernabei, Phys. Rev. Lett. 29, 1438 (1972); T. K. Chu, S. Bernabei, and R. W. Motley, Phys. Rev. Lett. 31, 211 (1973).
6. T. H. Stix, The Theory of Plasma Waves, Mc Graw-Hill, New York (1962).
7. V. E. Golant, Zh. Tekh. Fiz. 41, 2492 (1971) [Sov. Phys. Tech. Phys. 16, 1980 (1972)] .
8. S. Bernabei, W. M. Hooke, D. L. Jassby, and R. W. Motley, J. Appl. Phys. 46, 3286 (1975).
9. H. H. Kuehl, Phys. Fluids 5, 1095 (1962); R. K. Fisher and R. W. Gould, Phys. Fluids 14, 857 (1971); R. J. Briggs and R. R. Parker, Phys. Rev. Lett. 29, 852 (1972).
10. G. Francis, Ionization Phenomena in Gases, Butterworth's Scientific Publications, London (1960).
11. V. E. Golant, I. P. Gladkovskii, V. V. D'yachenko, M. M. Larionov, L. S. Levin, E. A. Mikhailov, V. V. Rozhdestvenskii, G. A. Serebrenyi and O. N. Shcherbinin, Proc. Vth Intern. Conference on Plasma Physics and Controlled Nuclear Fusion Research, Tokyo 1974, IAEA, Vienna, Vol. I, p. 231.
B. Bernabei, M. A. Heald, W. M. Hooke, and F. Paoloni, Phys. Rev. Letters 34, 866 (1975); R. R. Parker, private communication.
12. M. Brambilla, in Proceedings of the VIIth European Conference on Controlled Fusion and Plasma Physics, Vol. 2 (1975)
13. G. Grieger, W. Ohlendorf, H. D. Pacher, H. Wobig, G. H. Wolf, Proc. of the IVth Int. Conf. on Plasma Physics and Controlled Nuclear Fusion Research, Madison, USA, 1971, Vol. III, p. 37.

14. P.Javel, G.Müller, A.v.H.van Oordt, U.Weber, and R.R.Weynants, in Proceedings of the Seventh European Conference on Controlled Fusion and Plasma Physics. Vol.1, 147 (1975).
15. J.A.Schmidt, N.R.Sauthoff, and R.J.Hawugluk, Phys.Rev.Lett.33, 1272 (1974).
16. P.Javel, G.Müller, U.Weber and R.R.Weynants, Plasma Physics 18, 51 (1976).
17. P.M.Bellan and M.Porkolab, Phys.Fluids 17, 1592 (1974).
18. A.W.Trivelpiece and R.W.Gould, J.Appl.Phys. 30, 1784 (1959).
19. F.Leuterer, Plasma Physics 18, 453 (1976).
20. P.L.Colestock, Excitation and Propagation of Lower-Hybrid Waves in an Inhomogeneous, Bounded Plasma, Ph.D.Dissertation, Department of Engineering, University of Michigan, 1975.
21. M.Porkolab, V.Arunasalam and N.C.Luhmann, Jr., Plasma Physics, 17, 405 (1975)
22. E.Hinnov, A.S.Bishop and F.W.Hofmann, Princeton University, Plasma Physics Report MATT-270 (1964).
23. W.H.Louisell, Coupled Mode and Parametric Electronics, J.Wiley and Sons, New York (1960).
24. T.H.Stix, The Theory of Plasma Waves, Mc Graw-Hill, New York (1962), p.65.
25. C.F.F.Karney and A.Bers, Quarterly Progress Report No.113, Research Laboratory of Electronics, M.I.T., April 15, 1974, p.105.
26. P.D.Edgley, R.N.Franklin, S.M.Hamberger, and R.W.Motley, Phys.Rev.Lett. 34, 1269 (1975).
27. M.Porkolab, Phys.Fluids 17, 1432 (1974).
28. A.Rogister, Phys.Rev.Letters 34, 80 (1975).
29. M.Porkolab, private communication.
30. Spectroscopic measurements done by E.Hinnov and H.Ringler

Figure Captions

1. $\frac{\omega_{ce}}{\omega}$, $\frac{\omega_{pe}}{\omega}$ plane with existence region of electron plasma waves.
2. Experimental set-up of the W II a stellarator.
3. Line density vs absorbed power at different frequencies. The pressure is $p = 1.0 \cdot 10^{-5}$ torr. Also indicated are the expected values for a uniform profile of 6 cm width or a parabolic one of 9 cm. $B_0 = 5$ kG, $t = 0.11$.
4. Radial density profiles at $f_0 = 110$ MHz for various powers. $p = 3.5 \times 10^{-5}$ torr, $B_0 = 5$ kG, $t = 0.11$.
5. Density variation as a function of the rotational transform at three radial positions. The broken line gives the corresponding interferometer reading. $P = 170$ W, $p = 3.5 \cdot 10^{-5}$ torr, $f_0 = 200$ MHz, $B_0 = 5$ kG.
6. Typical electron temperature radial profiles. $f_0 = 35$ MHz, $p = 3.5 \times 10^{-5}$ torr, $B_0 = 5$ kG, $t = 0.11$.
7. Radial T_e profiles for different frequencies at constant power level. $P = 40$ W, $p = 3.5 \cdot 10^{-5}$ torr, $B_0 = 5$ kG, $t = 0.11$.
8. Axial variation of radial T_e profiles. $P = 100$ W, $f_0 = 50$ MHz.
9. Matching T_e and T_i profiles for different power at $f_0 = 35$ MHz. $p = 3.5 \cdot 10^{-5}$ torr, $B_0 = 5$ kG, $t = 0.11$.
10. Radial positions up to which the resonance cones can propagate as a function of rf power at $f_0 = 50$ MHz (○), 85 MHz (●) and 110 MHz (■). The probe is located at 58 cm from the source. The lines give the theoretical positions.
11. Radial distribution of rf potential amplitudes of the three waves present. $f_0 = 110$ MHz, $P = 70$ W, $p = 1.2 \cdot 10^{-5}$ torr, $B_0 = 5$ kG, $t = 0.11$.
12. Typical decay spectra at $f_0 = 200$ MHz for various magnetic field strengths. $P = 100$ W, $p = 2 \cdot 10^{-5}$ torr.
13. Amplitude of f_{ℓ} - component as a function of power at various pressures, pump frequency $f_0 = 200$ MHz, $B_0 = 4$ kG.
14. Low-frequency amplitude ϕ_{ℓ} vs side band amplitude ϕ_s for two pump frequencies $f_0 = 50$ MHz (○) and 110 MHz (▲). $B_0 = 5$ kG, $t = 0.11$, $p = 2.5 \cdot 10^{-5}$ torr.

15. $\int \phi_s^2 dr$ (●) vs power P. Also represented are the ion temperature increments T_i due to the instability, measured at 3 cm (O) and 4 cm (X) from the plasma centre. $f_o = 50$ MHz, $p = 3.5 \cdot 10^{-5}$ torr, $B_o = 5$ kG, $t = 0.11$.
16. T_i as a function of ϕ_s at $f_o = 50$ MHz (●) and 110 MHz (o). $p = 2 \cdot 10^{-5}$ torr, $B_o = 5$ kG, $t = 0.11$.
17. Diamagnetic signal N ($T_e + T_i$) as a function of applied pump frequency f_o . $P = 300$ W, $p = 1.25 \times 10^{-5}$ torr, $B_o = 5$ kG, $t = 0.11$. Also given is the overall source efficiency η .
18. Comparison of measured ion temperature with calculated values based on Pfirsch-Schlüter or plateau losses. The experimental points are obtained by the electrostatic analyzer (O), in which case the radial profiles are shown in the inset, or from the diamagnetism (●). $f_o = 200$ MHz, $p = 1.0 \times 10^{-5}$ torr, $B_o = 5$ kG, $t = 0.11$.
19. Two geometrical configurations for the wave vectors of the decay process.
20. Variation of threshold power (P_{thr}) and electron collision frequency ν_e on gas pressure. $f_o = 200$ MHz, $B_o = 4$ kG. The dashed line represents the contribution of ν_{en} only.
21. Theoretical dependence of growth rate γ_o on the pump field strength for dipole calculations involving quasimodes (●, o) and for EICW decay (full line).
22. Three-dimensional decay geometry. $\nabla_{g,s}$ is to be taken somewhere on the conical surface.

TABLE I

f_o [MHz]	P [W]	p [10^{-5} torr]	τ_p [μs]	T_i [eV]	NV 10^{15} partic	α %
110	40	3.5	500	2.0	1.2	75
110	80	3.5	500	2.5	1.65	59
110	57	1.25	700	2.9	1.35	62
50	60	3.5	500	3.6	0.6	22
50	125	3.5	500	5.0	0.8	18
35	60	3.5	500	6.0	0.4	15

Fig. 1

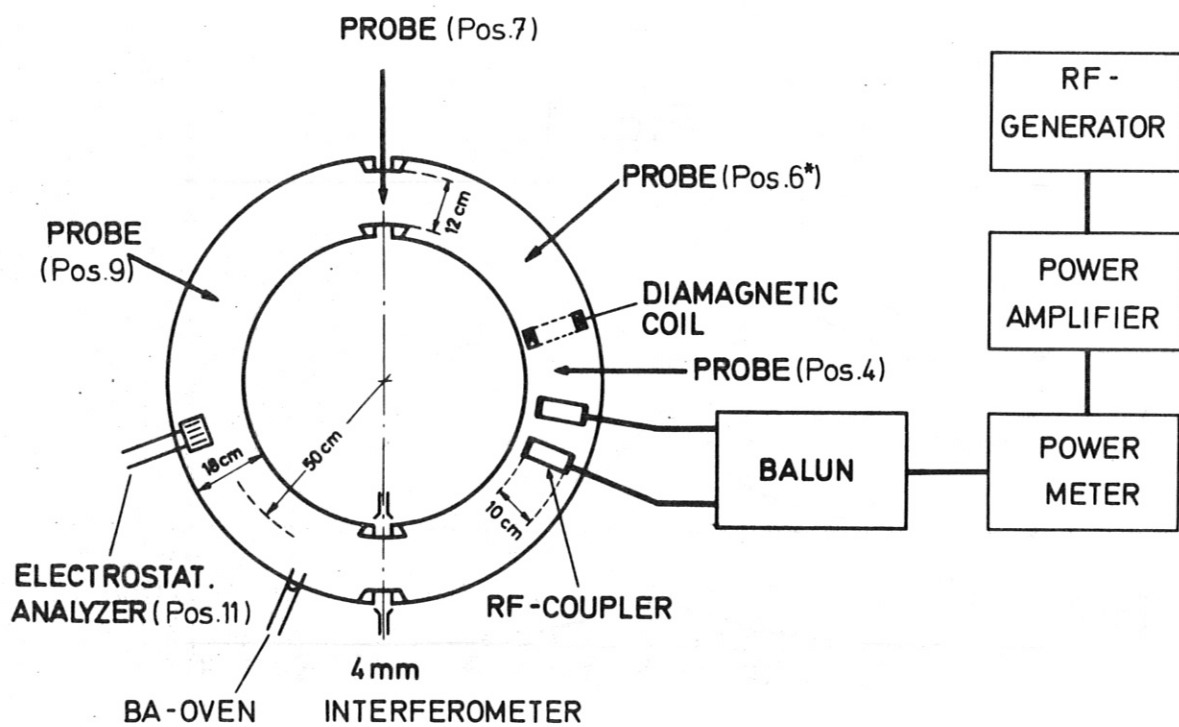
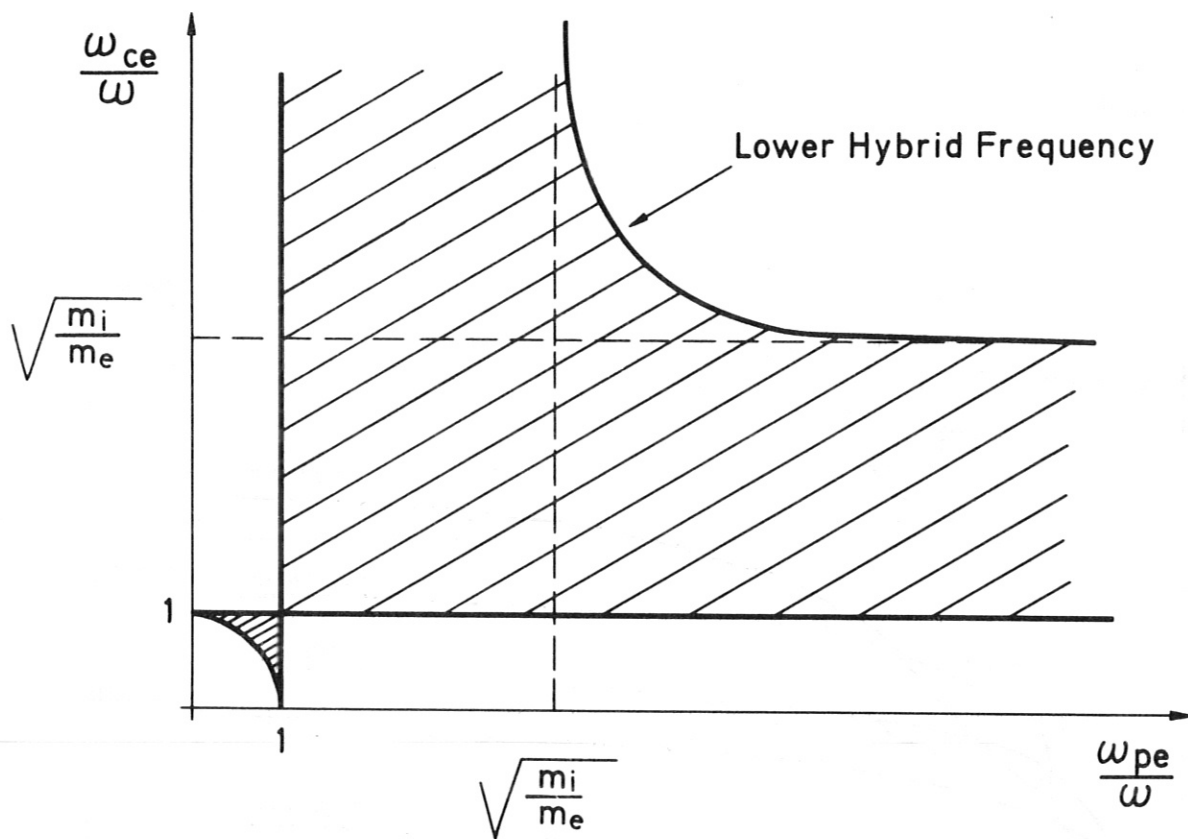


Fig. 2

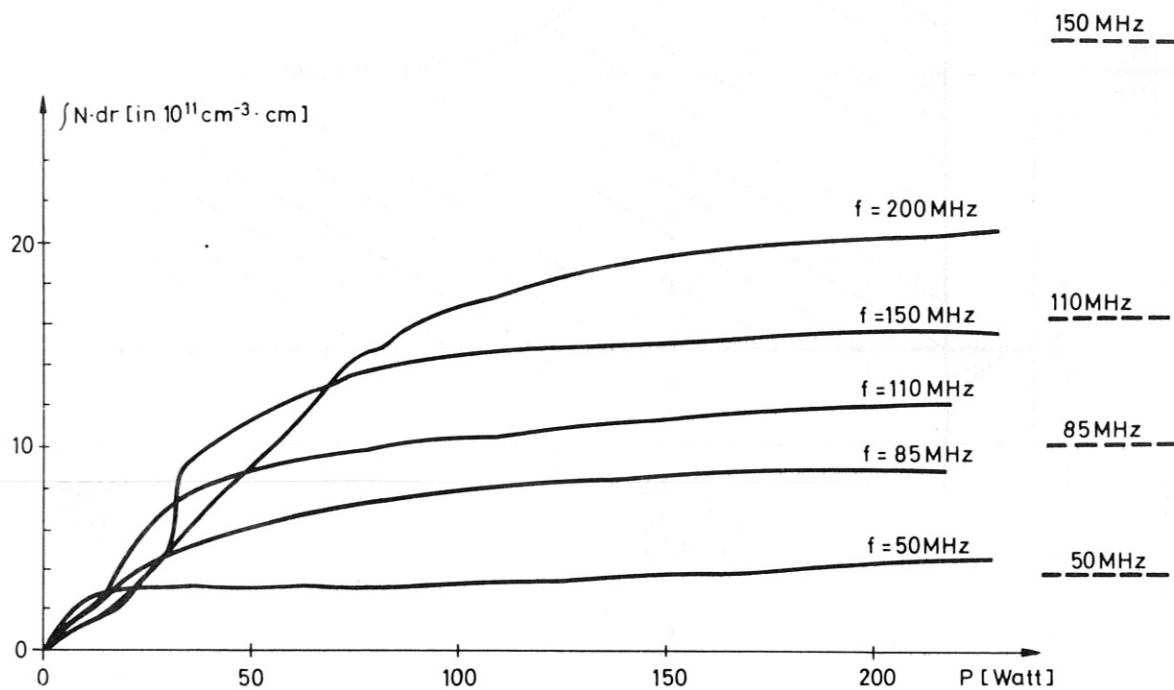


Fig. 3

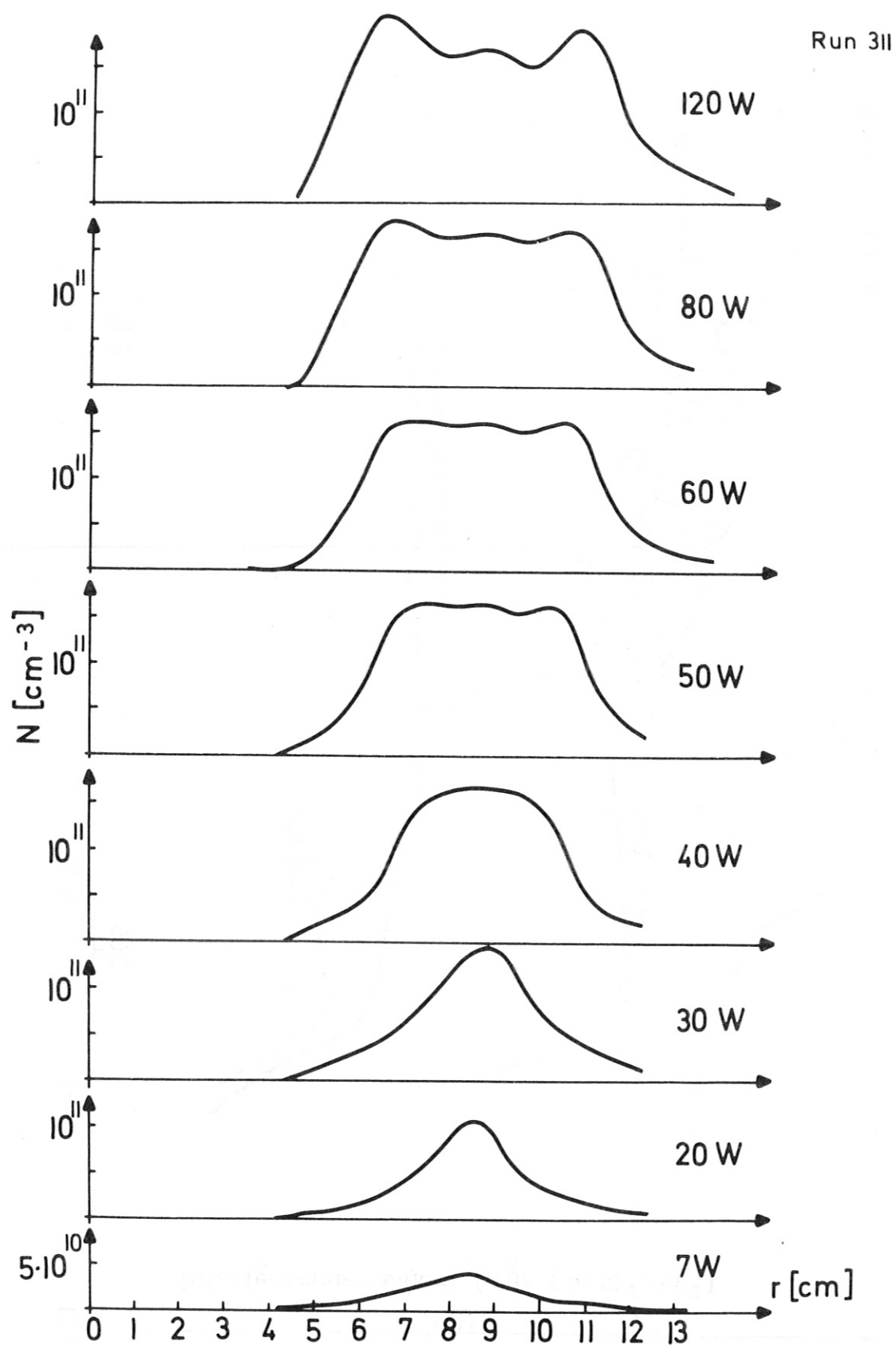


Fig. 4

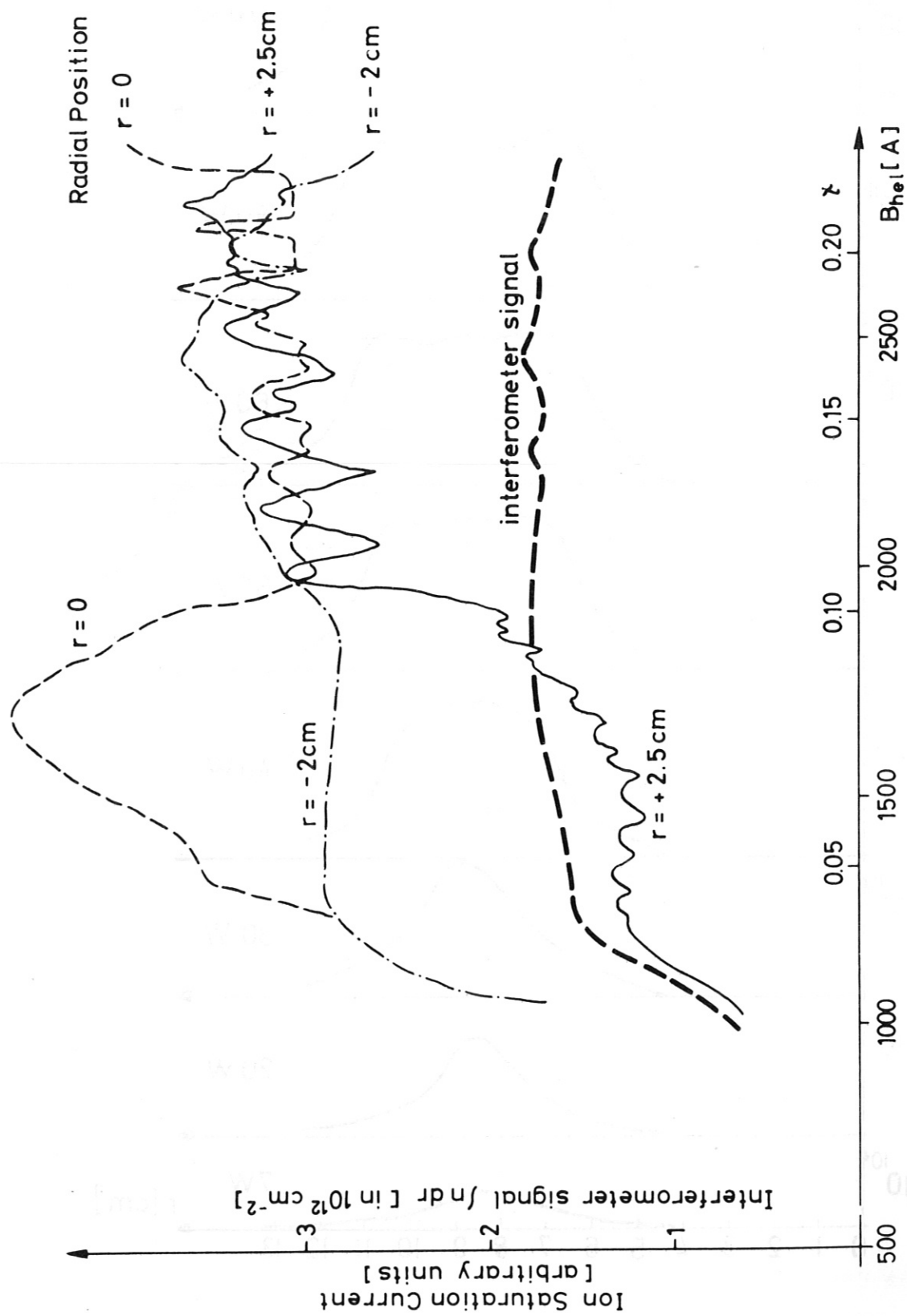
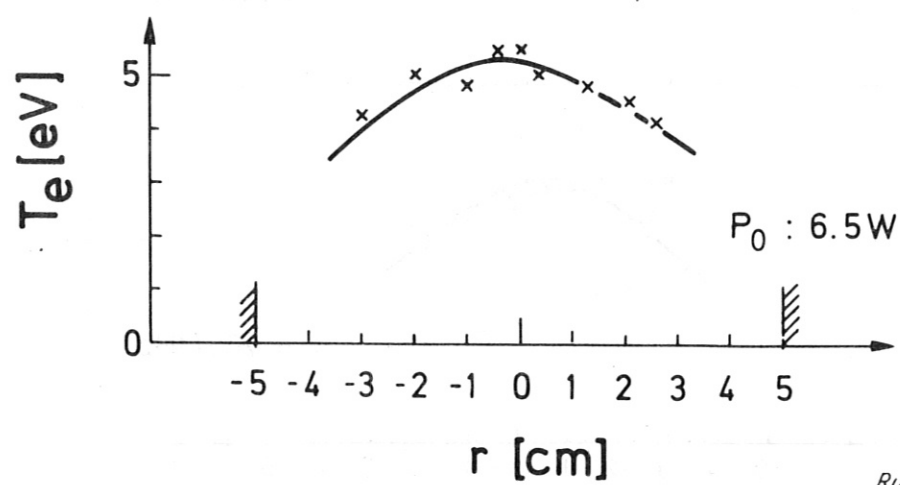
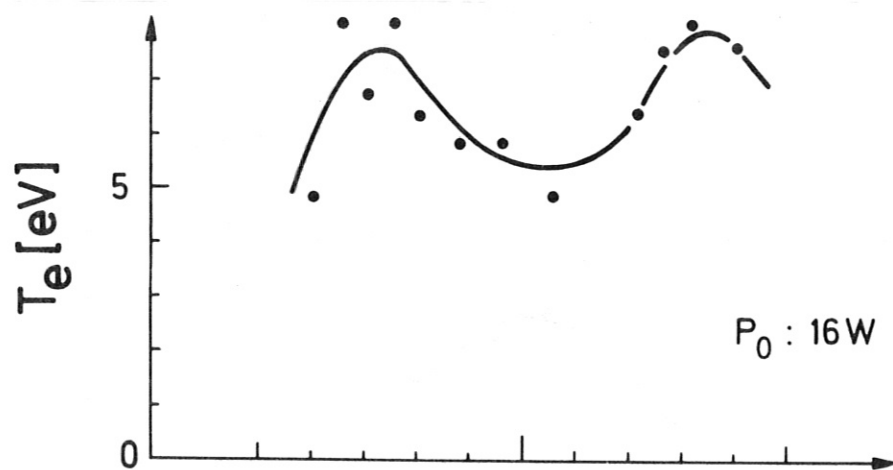
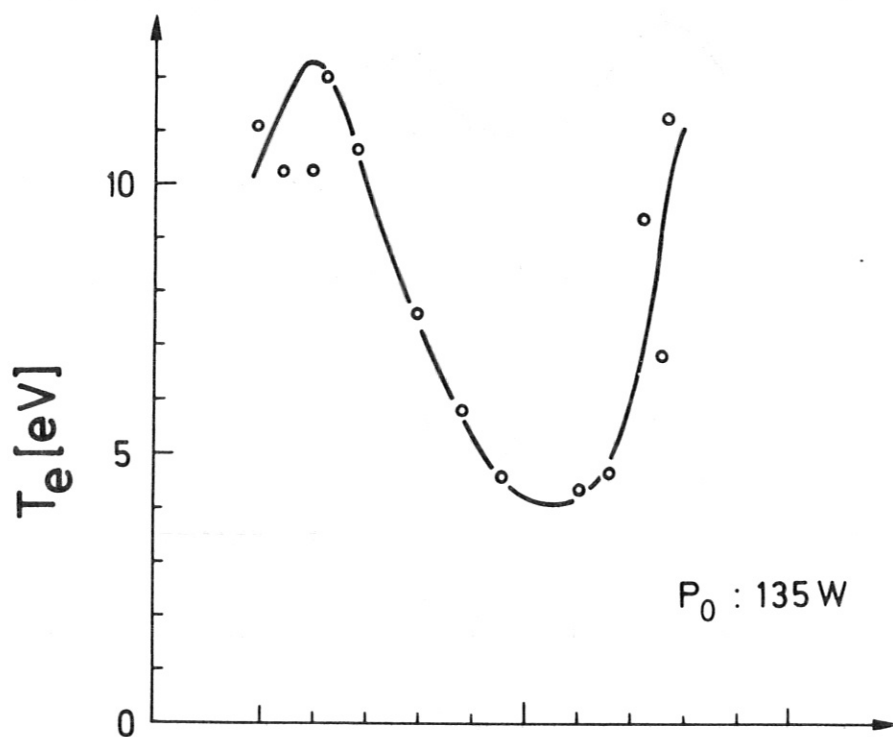
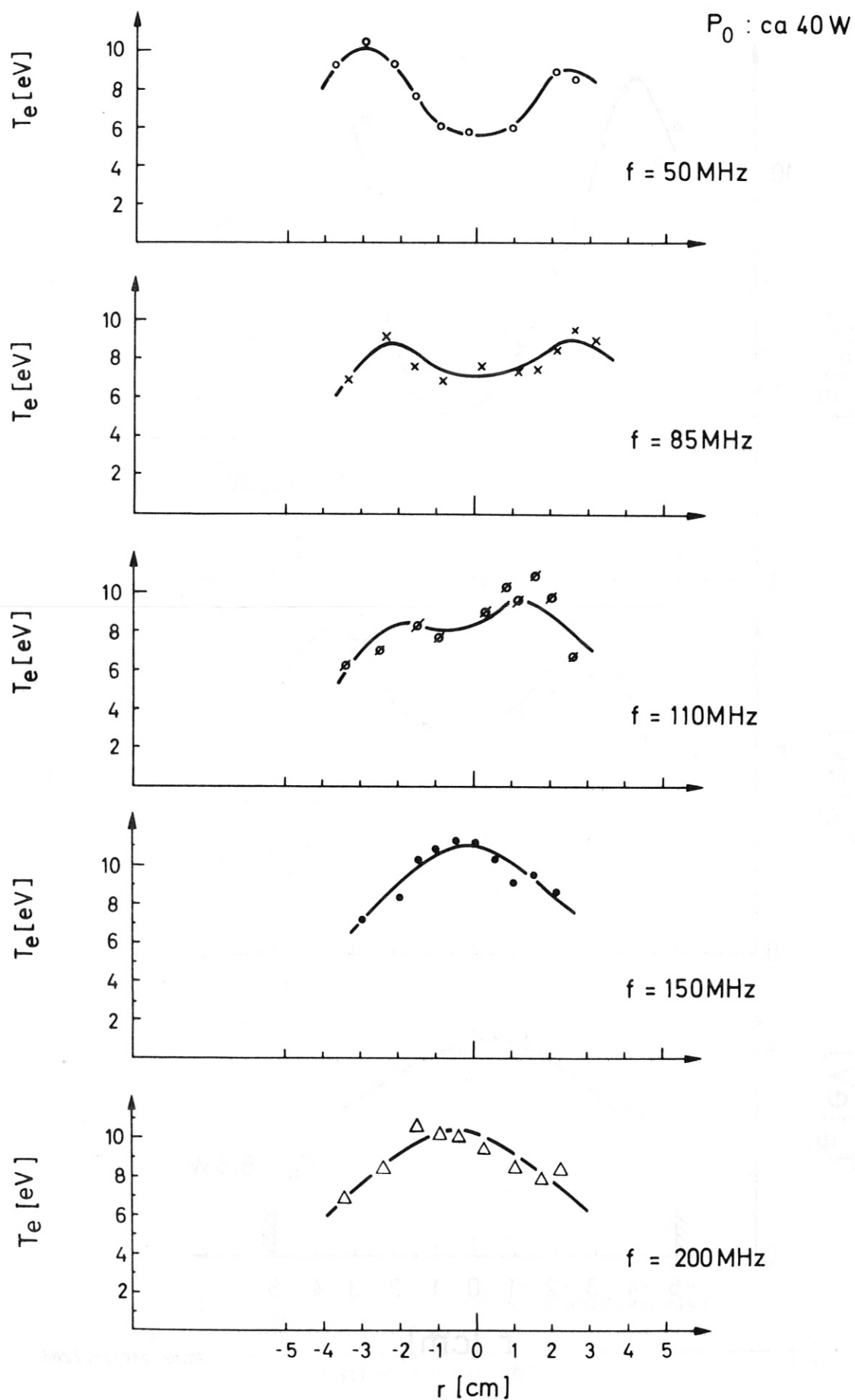


Fig. 5



Runs : 260/262/263

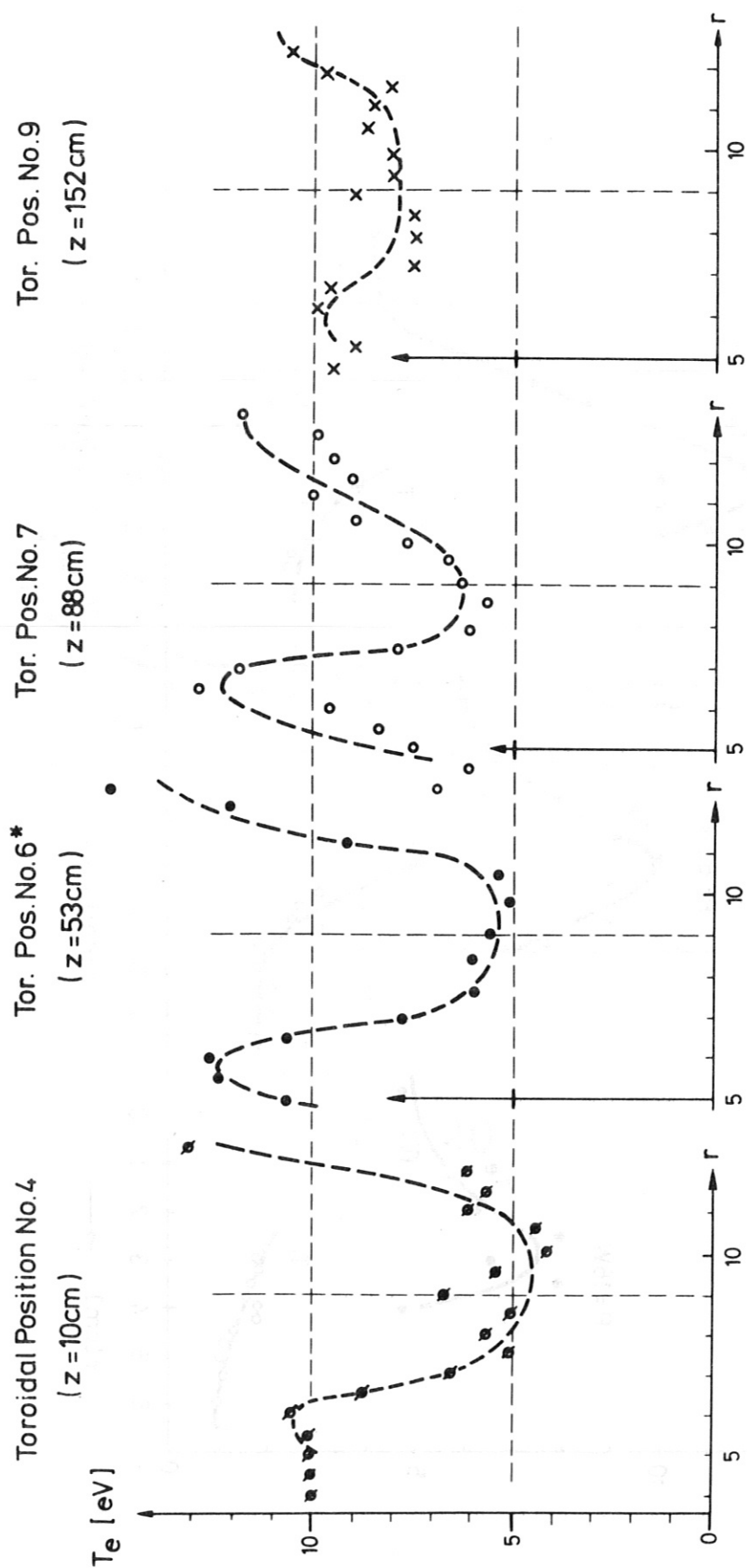
Fig. 6



runs: 241 - 246
19./20.11.74

Fig. 7

50MHz, 100W
 $P: 3.5 \times 10^{-5}$ Torr, H_2



Radial Positions r [cm]

Fig. 8

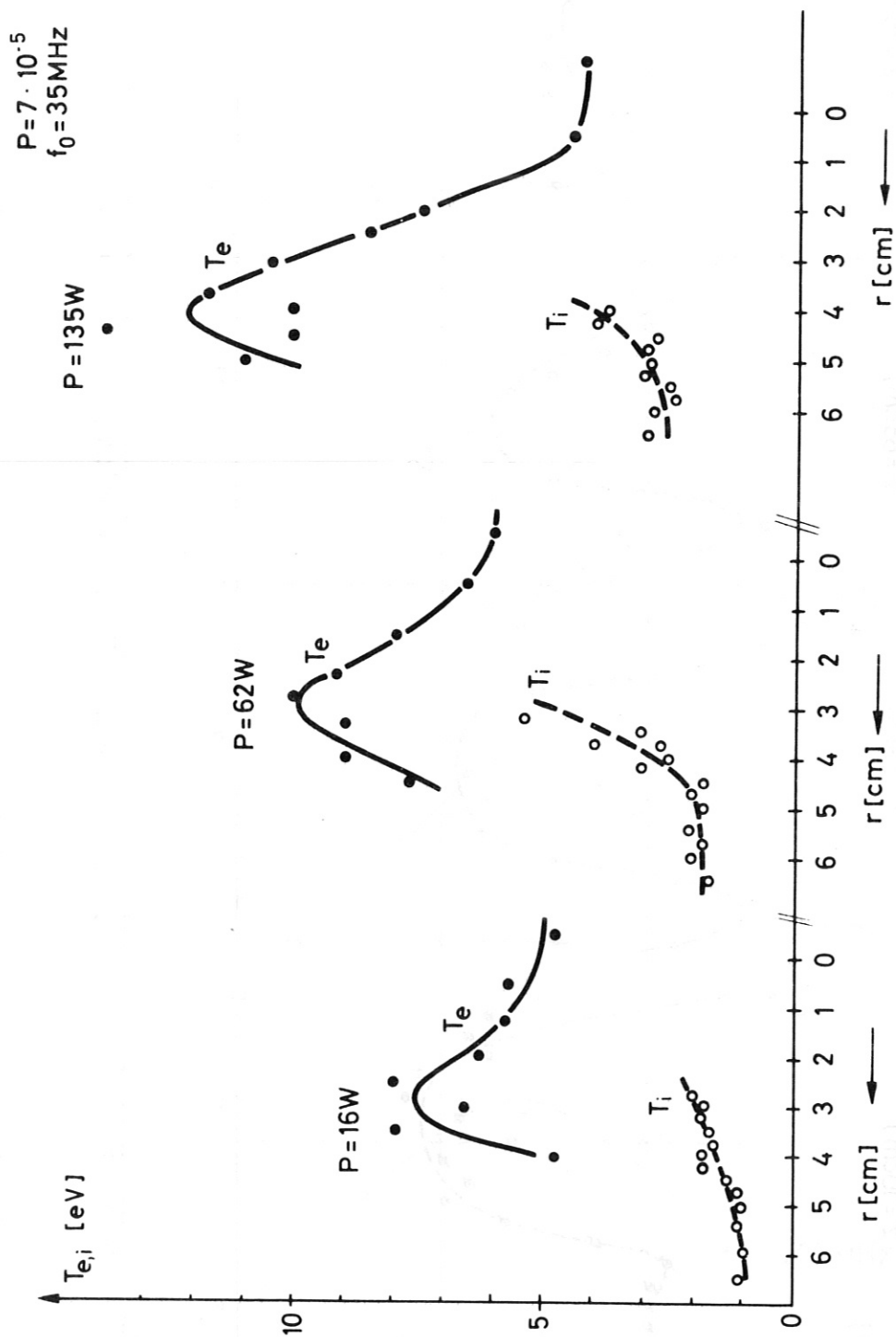


Fig. 9

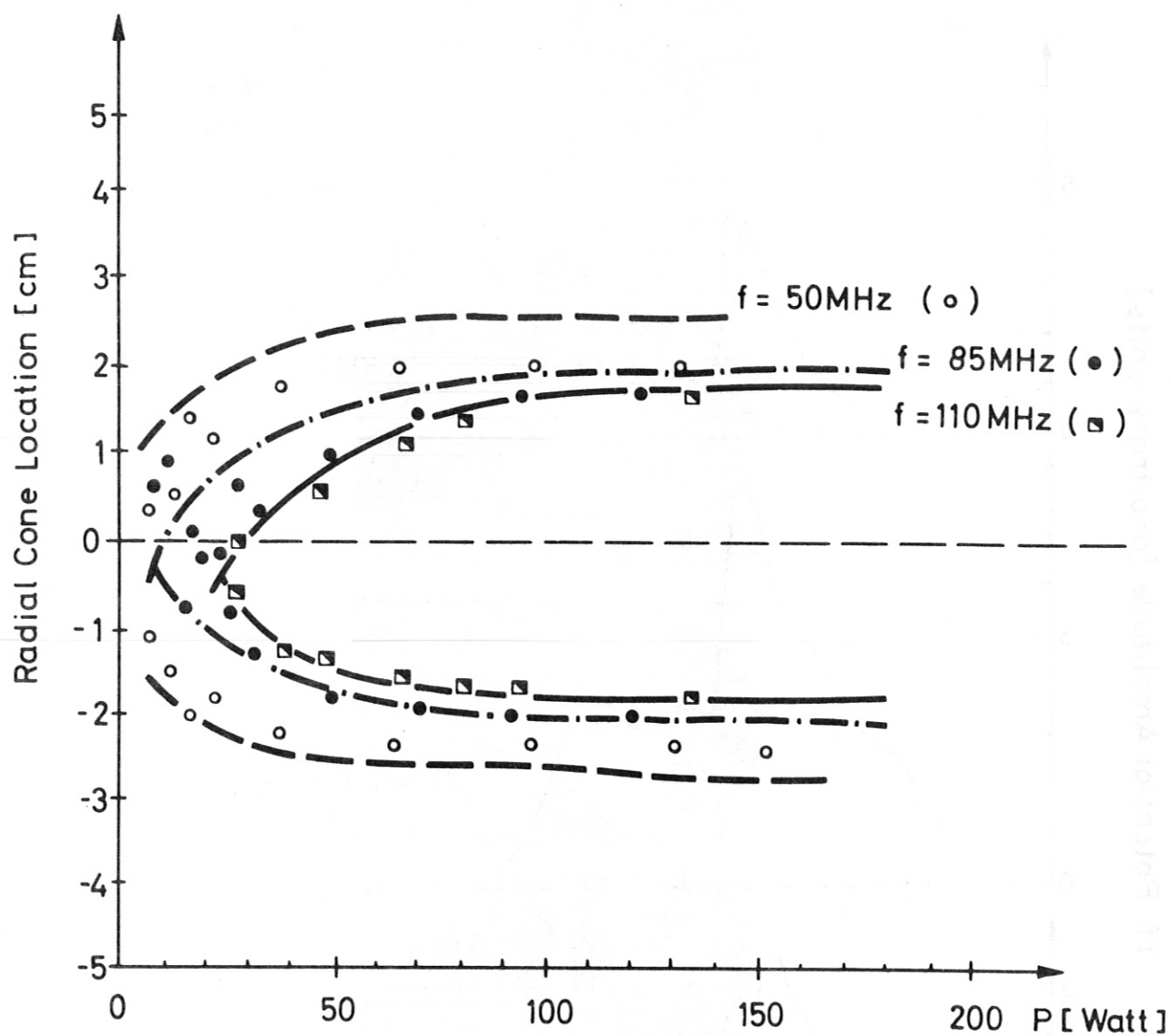
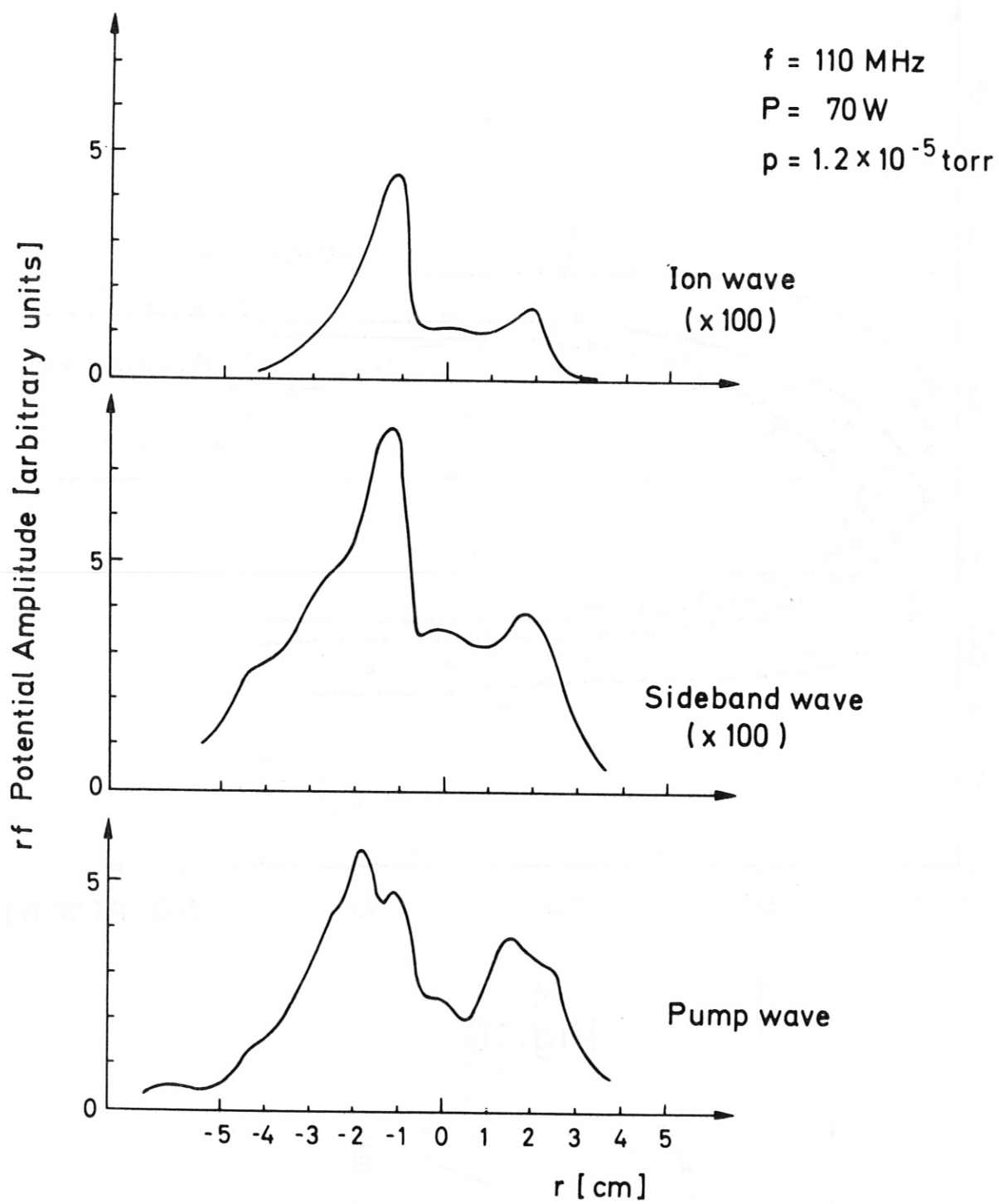
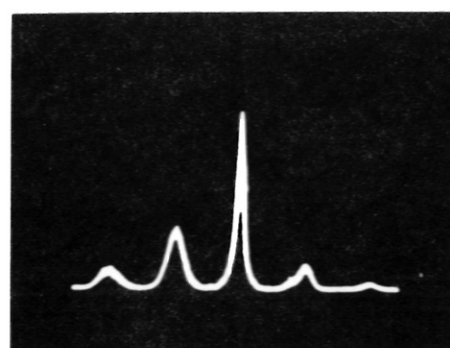


Fig. 10

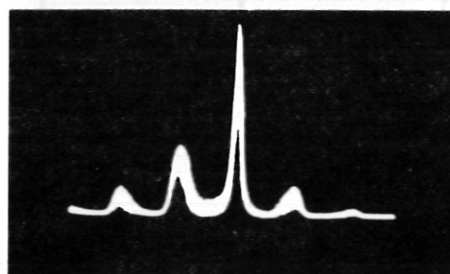


Run: 283

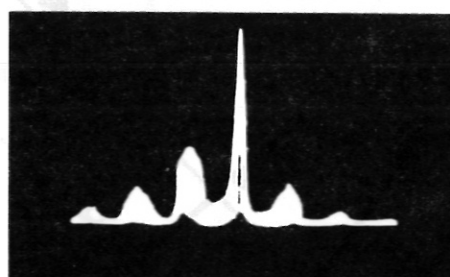
Fig. 11



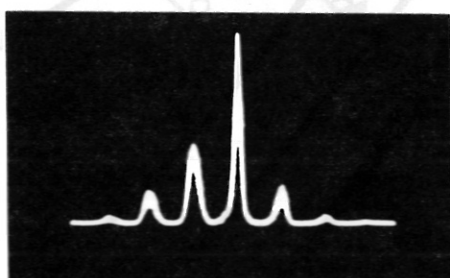
$B_t = 5,23 \text{ KG}$



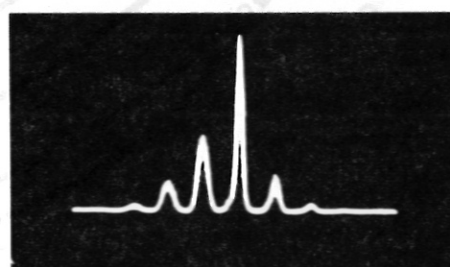
$B_t = 4,65 \text{ KG}$



$B_t = 4,07 \text{ KG}$



$B_t = 3,49 \text{ KG}$



$B_t = 2,91 \text{ KG}$

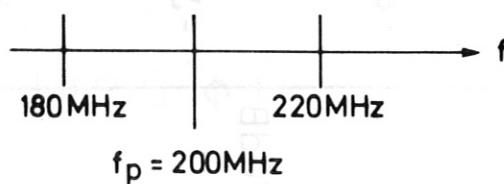


Fig. 12

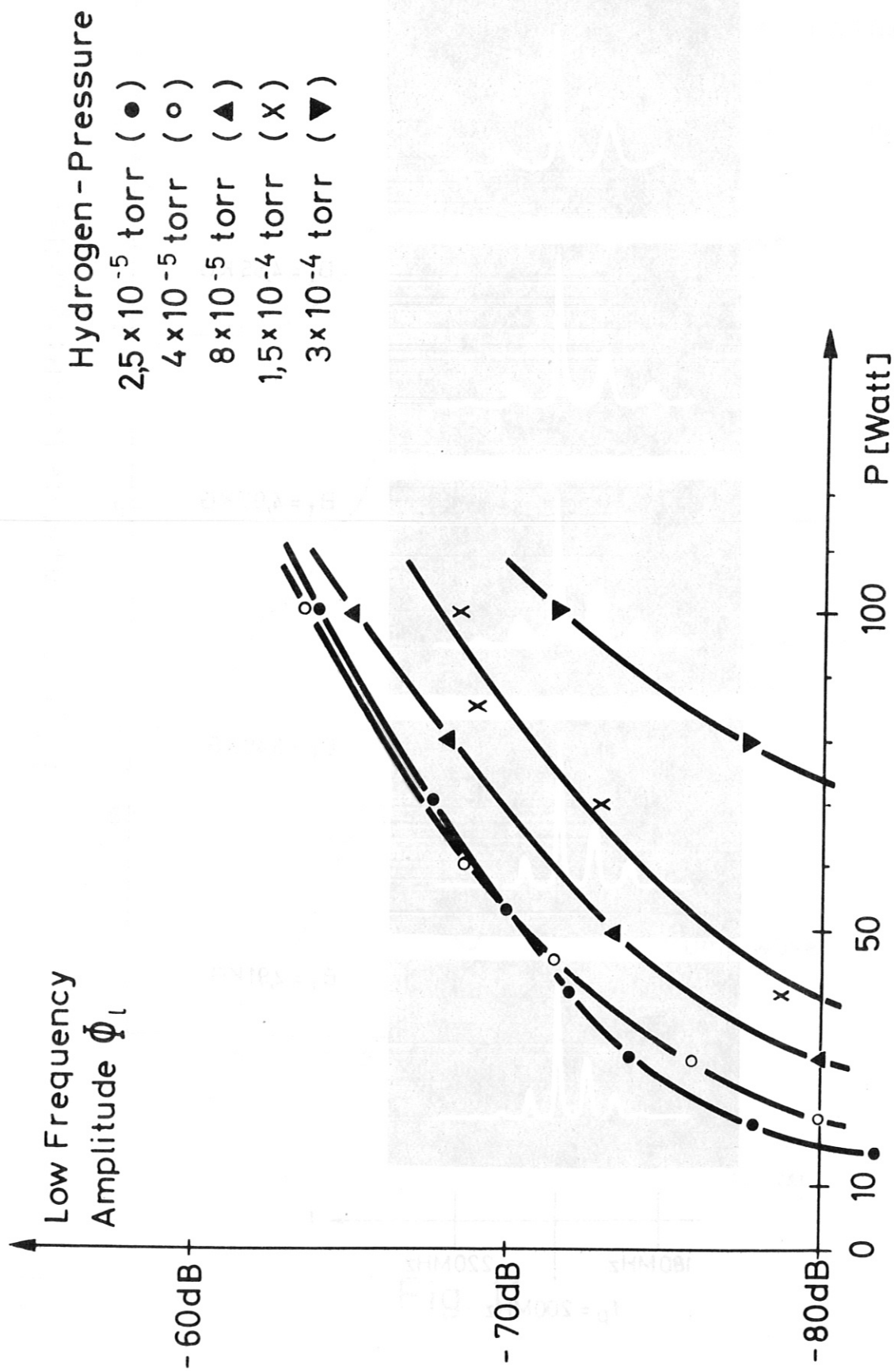


Fig. 13

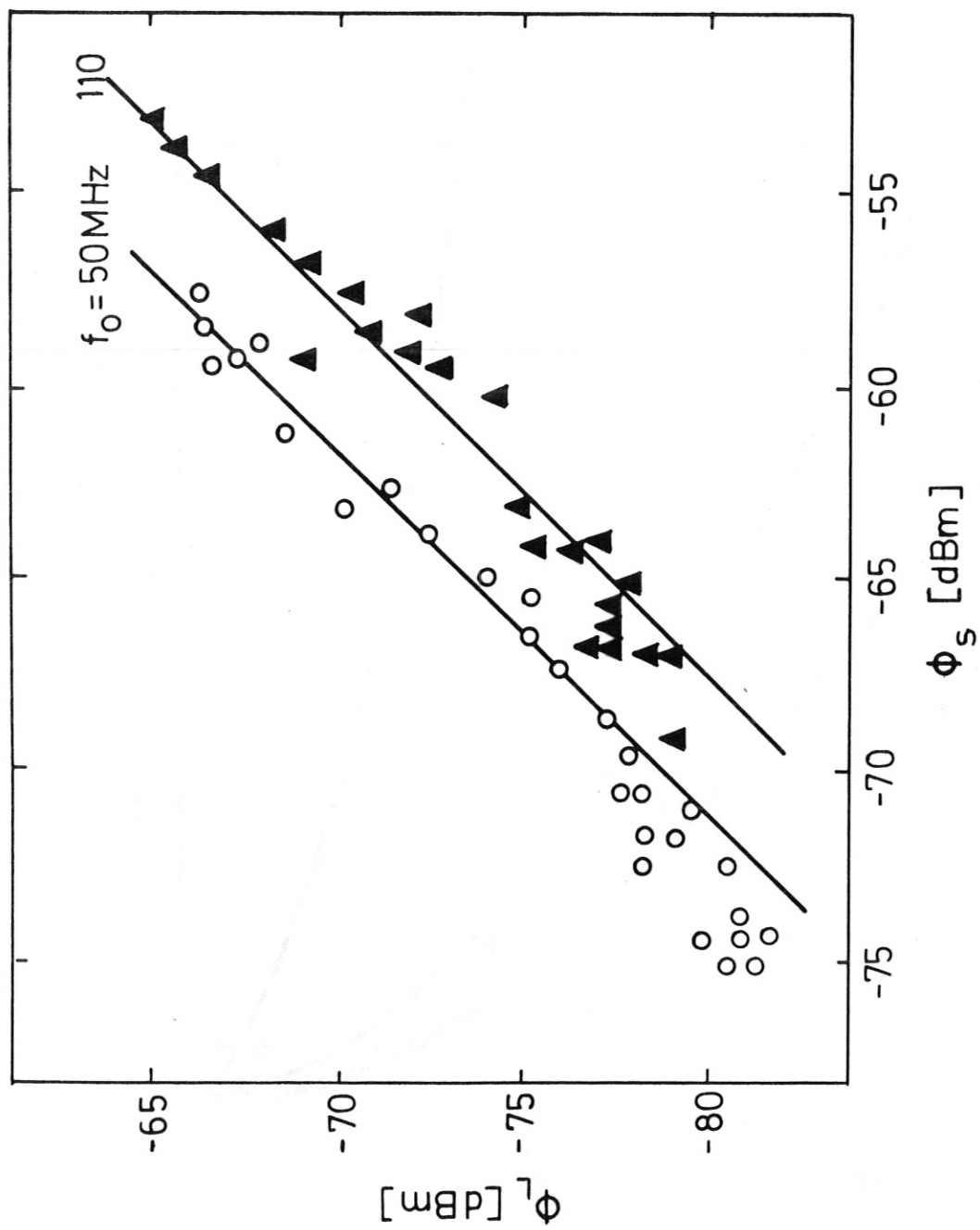


Fig. 14

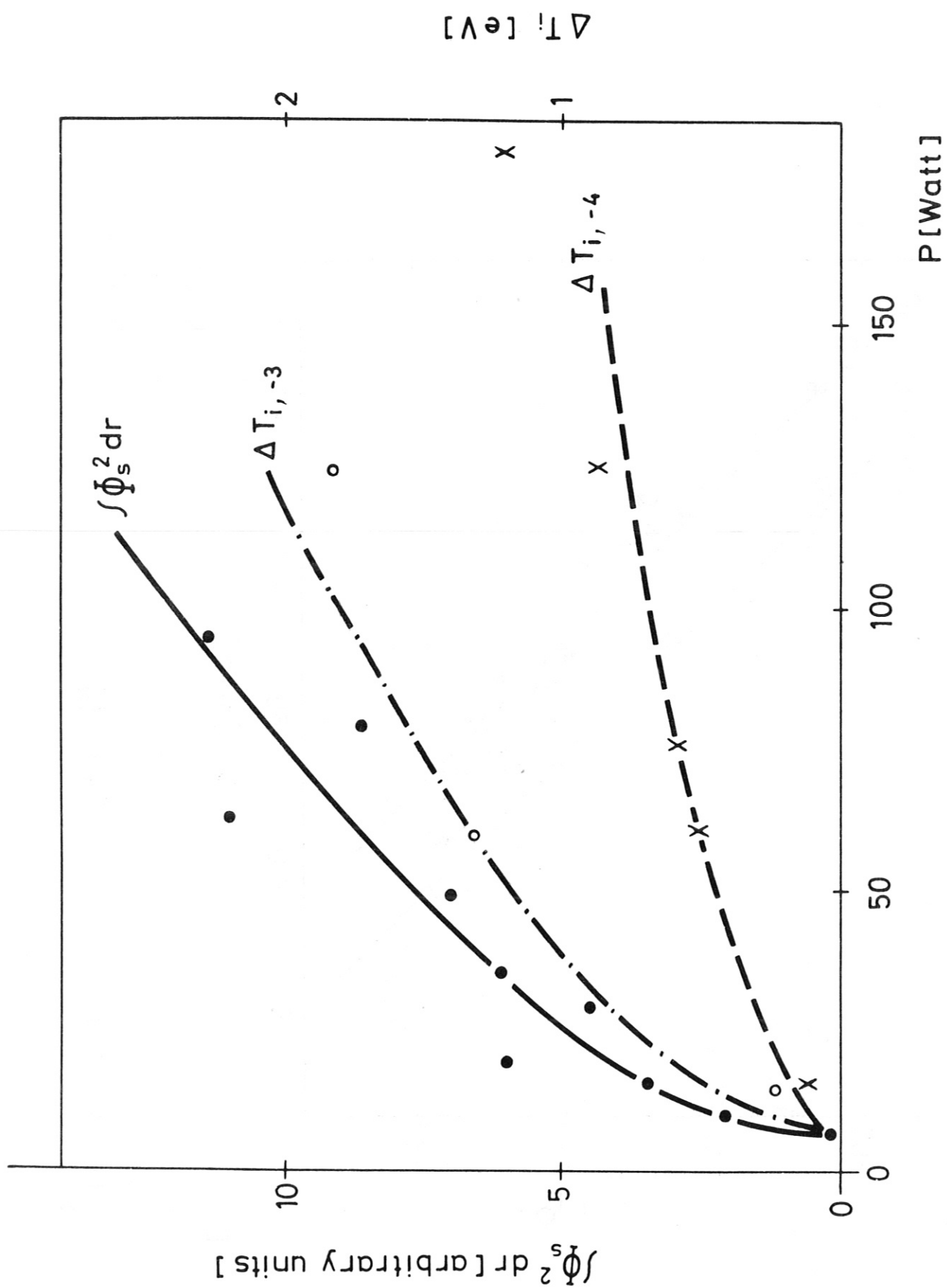


Fig. 15

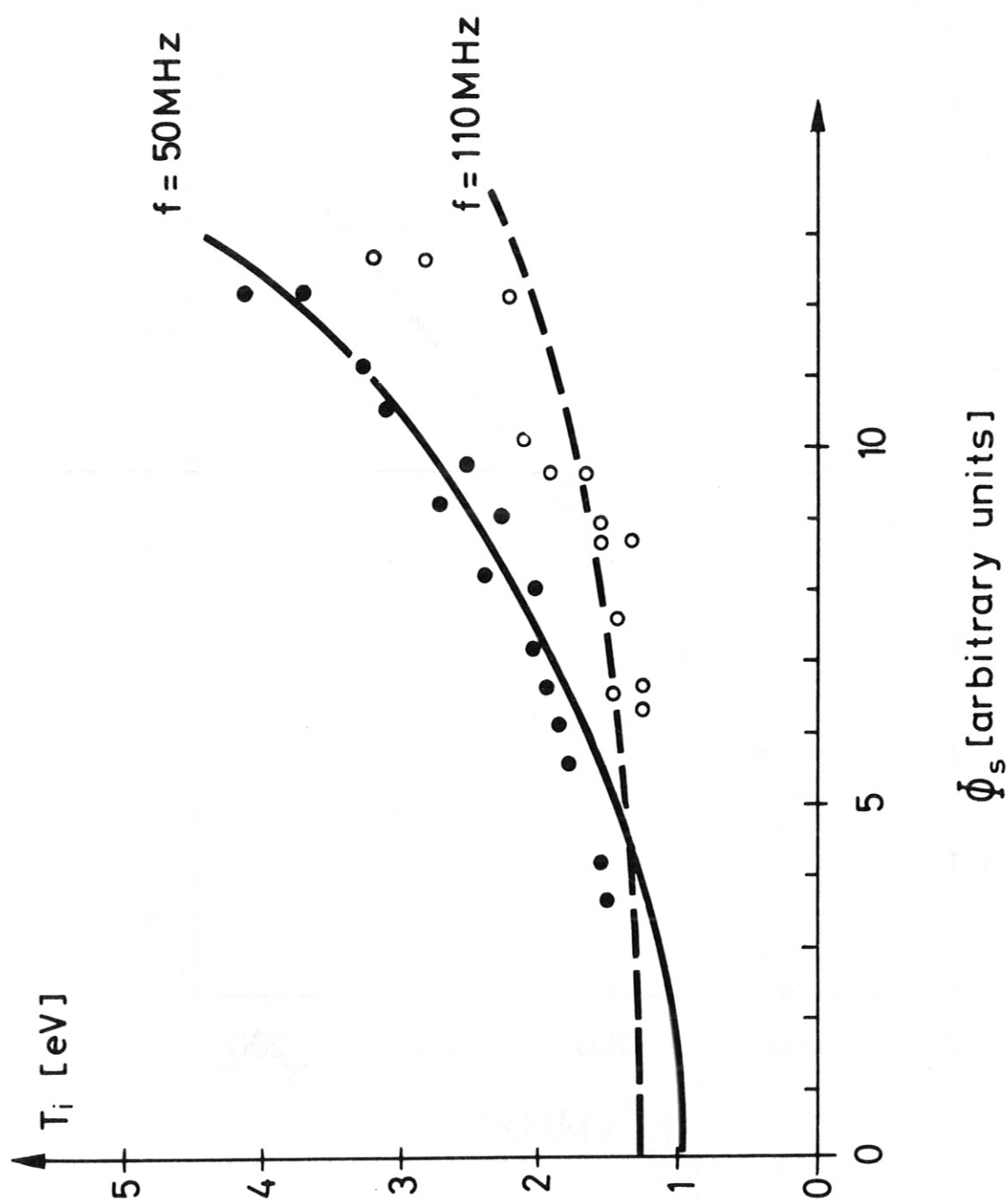


Fig.16

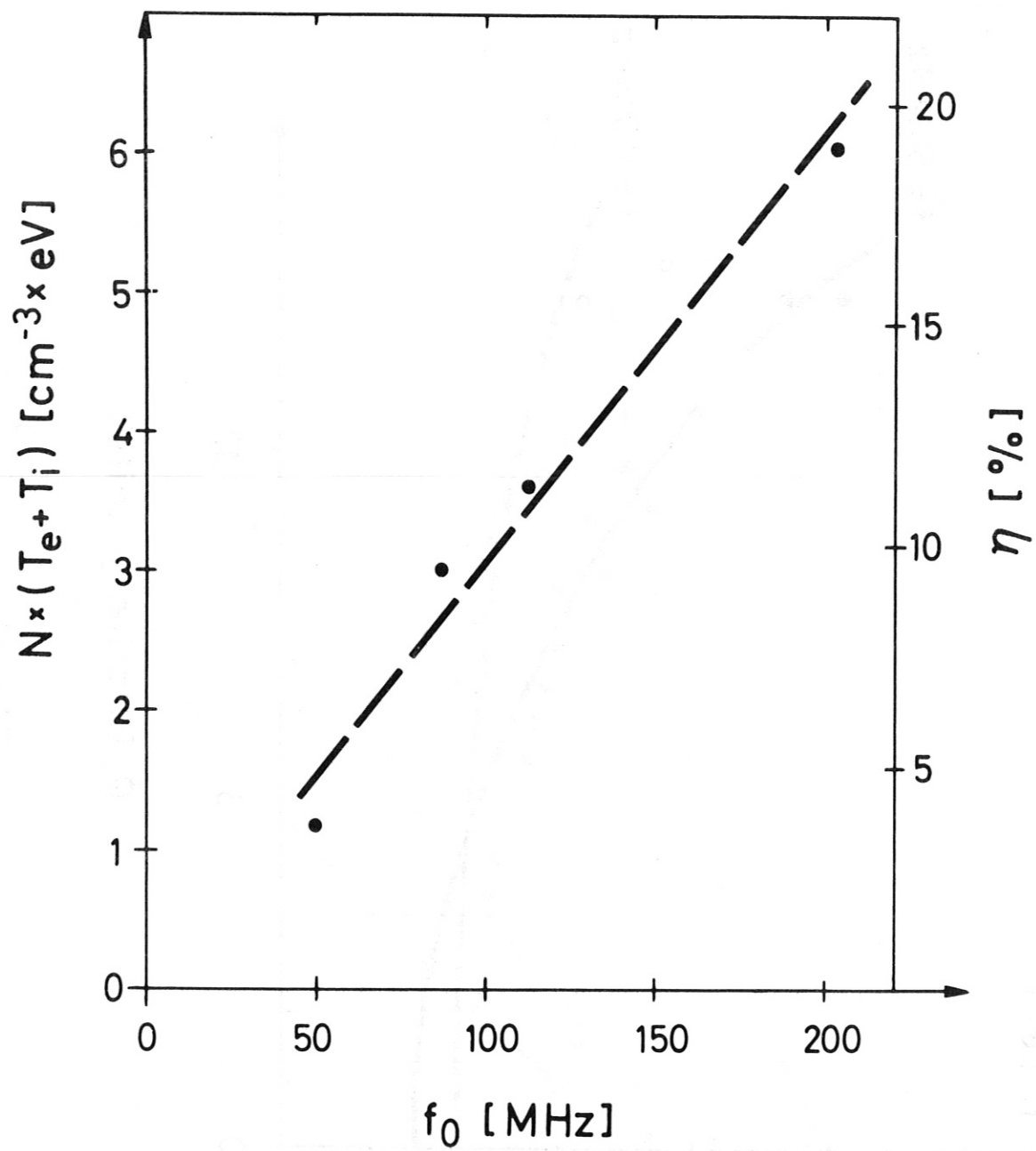


Fig. 17

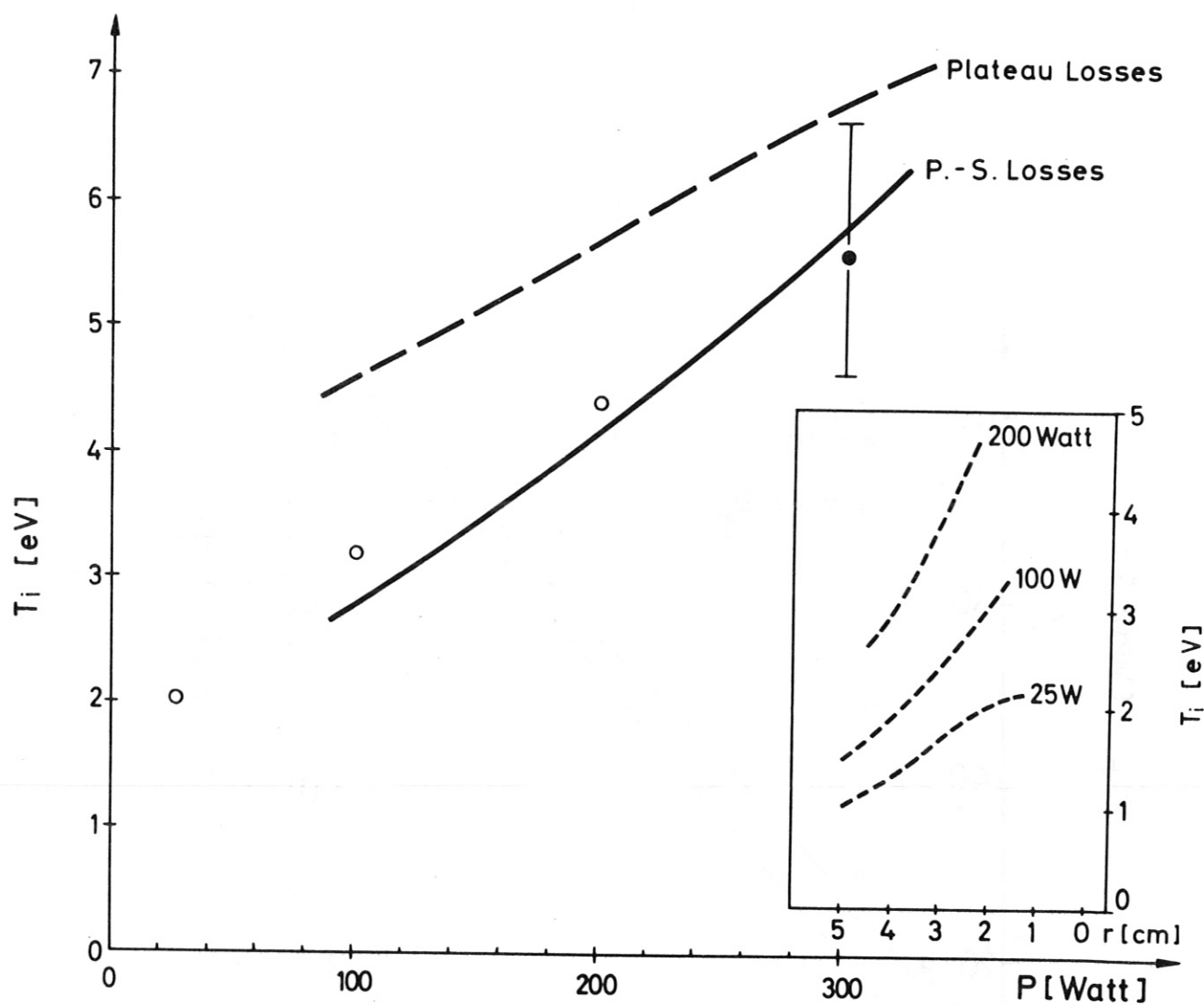


Fig. 18

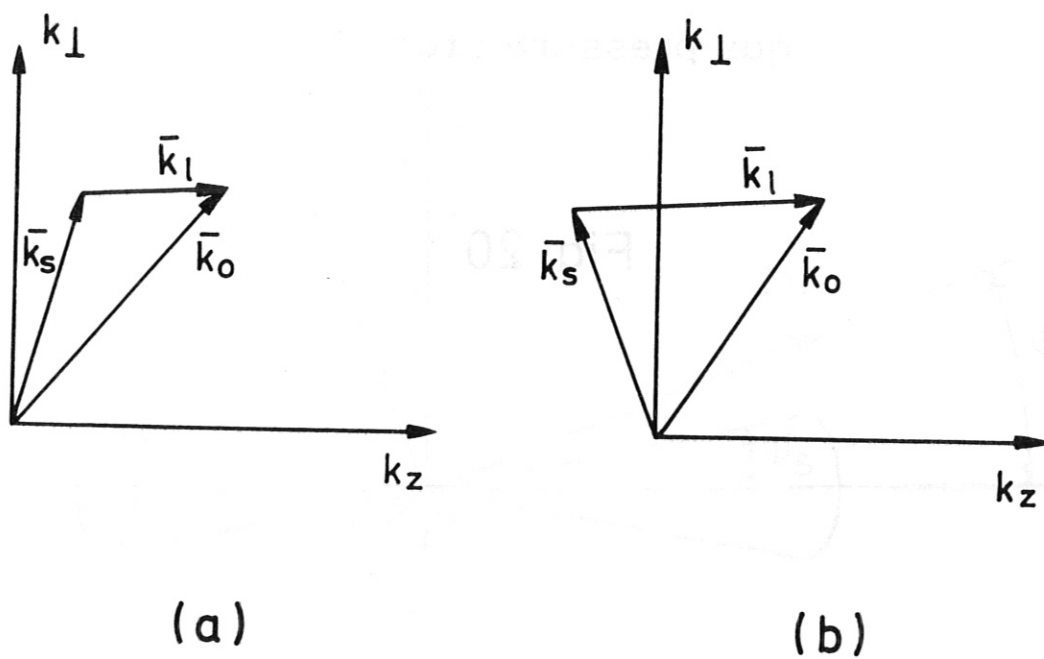


Fig. 19

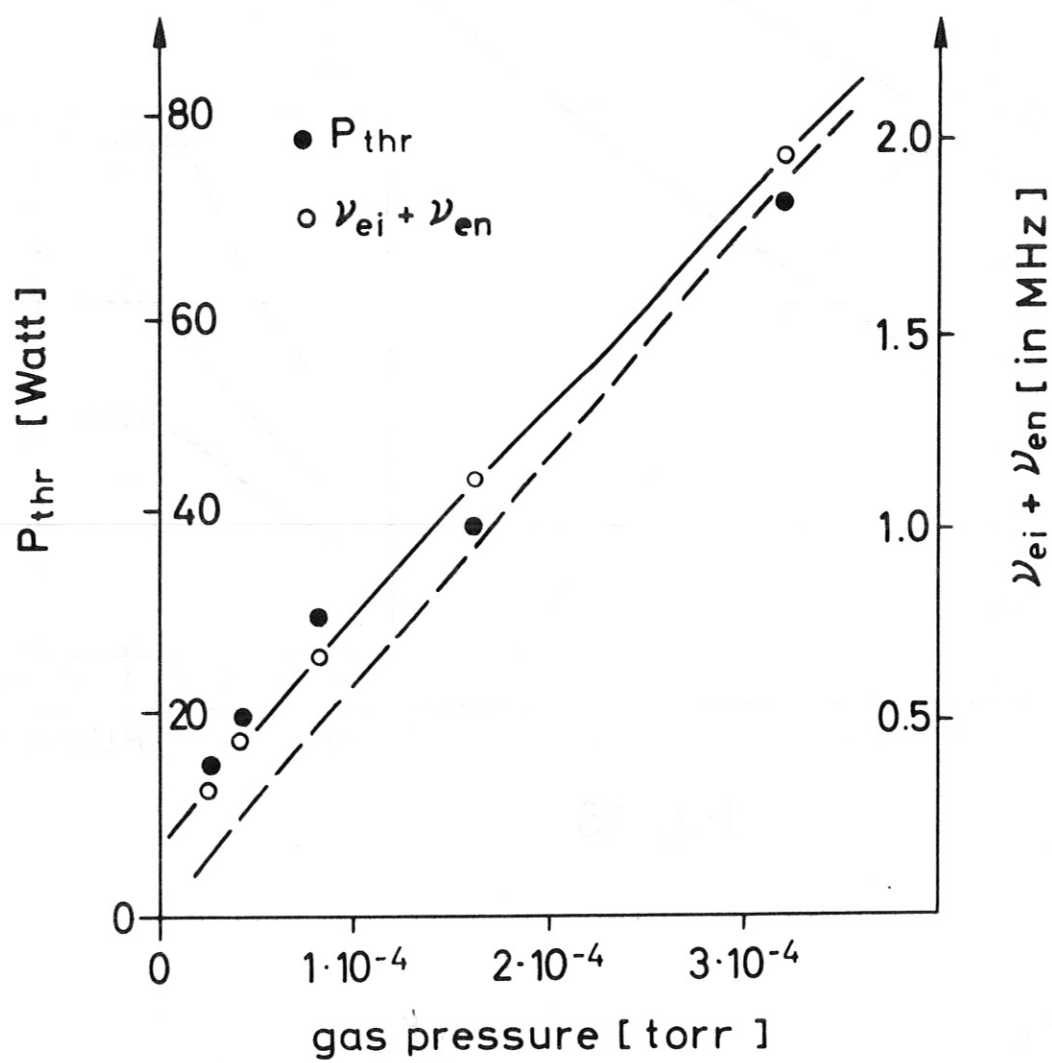


Fig. 20

Fig. 21

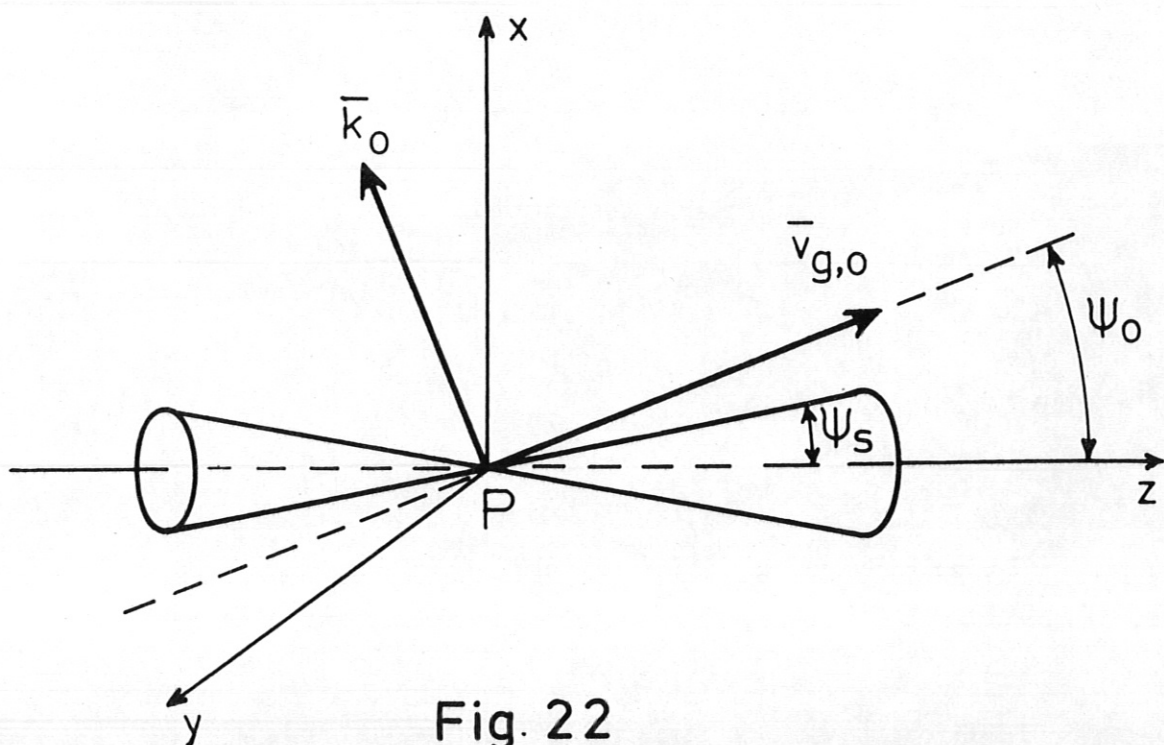
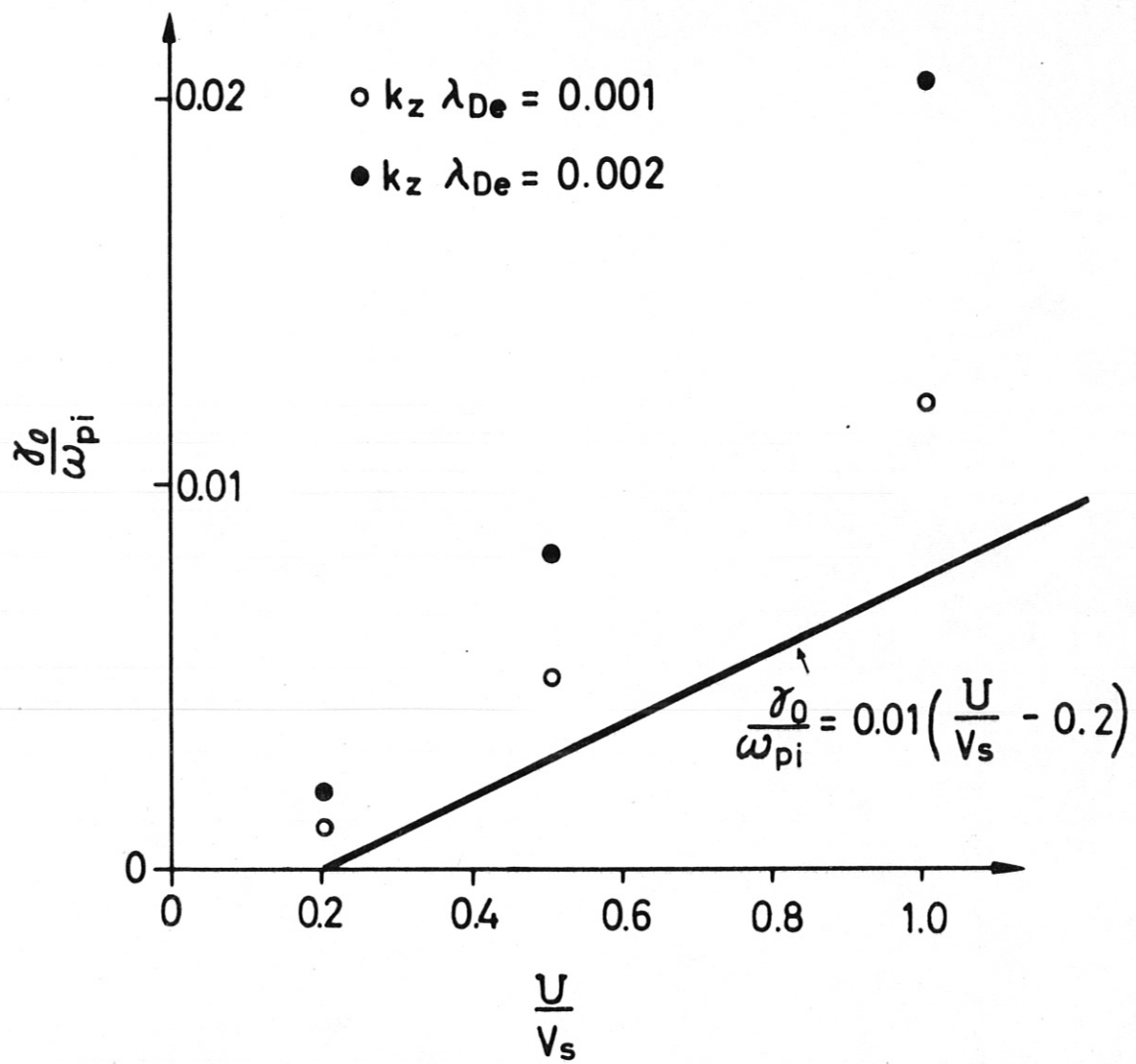


Fig. 22